STUDY OF 3-D FOURIER TRANSFORM PROFILOMETRY BY USING WAVELET FILTERS

Taweesak Chaiyakhan

A Thesis Submitted in partial Fulfillment of the Requirements for the Degree of Master of Science in Applied Physics

Suranaree University of Technology

Academic Year 2018

การศึกษาการแปลงฟูริเยร์โพรฟิโลเมทรีของรูปร่างสามมิติโดยการใช้ เวฟเลตฟิลเตอร์

นายทวีศักดิ์ ไชยขันธ์

วิทยานิพนธ์นี้เป็นส่วนหนึ่งของการศึกษาตามหลักสูตรปริญญาวิทยาศาสตรมหาบัณฑิต

สาขาวิชาฟิสิกส์ประยุกต์

มหาวิทยาลัยเทคโนโลยีสุรนารี

ปีการศึกษา 2561

STUDY OF 3-D FOURIER TRANSFORM PROFILOMETRY BY USING WAVELET FILTERS

Suranaree University of Technology has approved this thesis submitted in partial fulfillment of the requirements for a Master's Degree.

Thesis Examining Committee

____
(Assoc. Prof. Dr. Sirichok Jungthawan)
Chairperson

____
(Prof. Dr. Joewono Widjaja)
Member (Thesis Advisor)

____
(Asst. Prof. Dr. Panomsak Meemon)
Member

____
(Dr. Sukanya Tachathaiphop)
Member

____
(Prof. Dr. Santi Maensiri)
Vice Rector for Academic Affairs and Internationalization

____
(Assoc. Prof. Dr. Worawat Meevasana)
Dean of Institute of Science

ทวีศักดิ์ ไชยขันธ์ : การศึกษาการแปลงฟูริเยร์โพรฟิโลเมทรีของรูปร่างสามมิติโดยการใช้เวฟเลตฟิลเตอร์ (STUDY OF 3-D FOURIER TRANSFORM POFILOMETRY BY USING WAVELET FILTERS) อาจารย์ที่ปรึกษา : ศาสตราจารย์ ดร.ยูโวโน วิดจายา, 48 หน้า.

วิทยานิพนธ์เล่มนี้มุ่งเน้นในการศึกษาการแปลงฟูริเยร์โพรฟิโลเมทรีของรูปร่างสามมิติโดยการใช้เวฟเลตฟิลเตอร์ ได้แก่ อนุพันธ์อันดับที่หนึ่งของฟังก์ชันเกาส์เซียน, เมกซิกันแฮต และ มอร์เลตเวฟเลต โดยใช้วัตถุรูปทรงสามเหลี่ยมสำหรับการศึกษา ผลกระทบจากการเปลี่ยนจุดศูนย์กลางและความกว้างของฟิลเตอร์ที่มีผลต่อการสร้างรูปสามมิติได้รับการตรวจสอบประสิทธิภาพ ในการสร้างรูปสามมิติ จุดศูนย์กลางของฟิลเตอร์และความถี่พื้นฐานของเกรตติงบนผิวของวัตถุจะถูกกำหนดให้ตรงกัน ประสิทธิภาพของทั้งสามเวฟเลตฟิลเตอร์จะได้รับการประเมิน โดยการนำไปเทียบกับความสูงของวัตถุที่ได้จากการวัดโดยตรง ผลจากการทดสอบชี้ให้เห็นว่า ผลจากเมกซิกันแฮตสามารถสร้างจุดยอดของวัตถุได้เป็นอย่างดี เนื่องด้วยกระบวนการเปลี่ยนกลับของฟิลเตอร์ที่มีความกว้างมากกว่า ในขณะที่มอร์เลตเวฟเลตมีความคลาดเคลื่อนของความสูงเฉลี่ยของวัตถุน้อยที่สุด เนื่องจากมีความกว้างของฟิลเตอร์ที่เหมาะสมและเป็นอิสระจากการเปลี่ยนจุดศูนย์กลางของฟิลเตอร์

สาขาวิชาฟิสิกส์ ลายมือชื่อนักศึกษา____________

ปีการศึกษา 2561 ลายมือชื่ออาจารย์ที่ปรึกษา____________

TAWEESAK CHAIYAKHAN: STUDY OF 3-D FOURIER TRANSFORM PROFILOMETRY BY USING WAVELET FILTERS. THESIS ADVISOR: PROF. JOEWONO WIDJAJA, Ph.D. 48 PP.

FOURIER TRANSFORM PROFILOMETRY/3D SHAPE MEASUREMENT/ WAVELET TRANSFORM/WAVELET FILTER/GRATING PROJECTION

The work in this thesis focuses on the study of 3-D Fourier transform profilometry using wavelet filters that are the first-order derivative of Gaussian, the Mexican hat and the Morlet wavelets and an isosceles prism as a test object. Effects of the filter center frequency and its passband on the 3-D reconstruction performance are experimentally investigated. To reconstruct the object profile, the center frequency must match to that of the fundamental spectrum of the deformed grating patterns. The reconstruction performance of the three wavelets is quantitatively evaluated by comparing the reconstructed height with that obtained by using a direct contact measurement. The experimental results show that the Mexican hat wavelet can reconstruct sharp prism peak due to its broad passband with quadratic response in both transition bands. It is also found that the Morlet wavelet has the lowest average error in the height measurements, because it has well localized passband, which can be independently defined without affecting its center frequency.

School of Physics — Student's Signature ____________________

Academic Year 2018 — Advisor's Signature ____________________

ACKNOWLEDGEMENTS

My thesis could not be accomplished without much help and support from many people. First of all, I am grateful to my advisor, Prof. Dr. Joewono Widjaja for excellent support throughout the course of this research, whether it be the study and teaching, the research process and the methodology, but also lifestyle guidelines. I would not have achieve this far without his support.

I am grateful to the thesis defense committee, Assoc. Prof. Dr. Sirichok Jungthawan, Asst. Prof. Dr. Panomsak Meemon and Dr. Sukanya Tachathaiphop in the School of Physics, Suranaree University of Technology for their comments and suggestions. Also, I would like to thank Suranaree University of Technology and Institute of Research and development for a thesis support scholarship.

I would like also to thank Dr. Porntip Chuamchaitrakool for her advice and suggestion when I had problems. Mr. Jaroon Wongjarern for providing experimental data and technical suggestion.

Finally, I most gratefully my family and my friends for their support and encouragement.

Taweesak Chaiyakhan

CONTENTS

CONTENTS (Continued)

LIST OF TABLES

LIST OF FIGURES

LIST OF FIGURES (Continued)

LIST OF FIGURES (Continued)

Figure **Page**

LIST OF FIGURES (Continued)

Figure **Page**

CHAPTER I

INTRODUCTION

1.1 Background

Fourier transform profilometry (FTP) is one of the optical methods for measuring three-dimensional (3-D) shape of objects (Takeda *et al*., 1982; Takeda and Mutoh, 1983). In the FTP method, Ronchi grating pattern is subsequently projected onto an object surface and a flat reference plane. Their deformed patterns are recorded by using a camera. The deformation gives modulation of the grating phase by height profiles. To reconstruct the object profile, this phase information is extracted from the fundamental spectrum of the deformed grating by using Fourier transformation. However, the existence of a zero-order spectral component corrupts the desired phase information of the fundamental spectrum. To solve this problem, this spectrum is filtered out by using a rectangular band-pass filter. Since the rectangular filter has a sharp frequency response, the 3-D height profile reconstructed by using the conventional FTP may suffer from ringing artifacts, as a result, fine details of the surface profile are degraded. This is an inherent limitation of the conventional FTP.

The FTP technique has been applied to the 3-D reconstruction of object surfaces having fine and coarse topographies. In dermatology, the FTP has been used for monitoring facial skins after laser-based skin treatment (Lalos *et al*., 2015). The skin topography measurement system was implemented by using a digital single-lens reflex

(DSLR) camera with its built-in flash as a light illumination source of Ronchi grating. The whole optical system weighted 1500 g and measured 270 mm $\times$ 135 mm $\times$ 160 mm, making it convenient to be employed as a handheld device. The FTP technique was used to reconstruct 360° the surface boundary of the object specimen for fluorescence molecular tomography (FMT) measurement in biomedical fields (Shi *et al*., 2013). It is a fact that although the FMT is promising *in vivo* tool for detection and diagnosis of diseases, the FMT cannot provide a 3-D surface profile of the object specimen as a boundary constraint. Although other computed tomography technology is available (Guo *et al*., 2010), it cannot be easily combined with the FMT system due to space and time limitations. In this application, the FTP was firstly used to reconstruct 360° the surface profile of the object. This full angle surface reconstruction was obtained by taking multiple frames of grating deformed by the object rotated at different angles. After the FMT measurement, the FTP reconstructed surface boundary was superimposed over the fluorescence image. As a result, the depth information of fluorochrome distribution in the object tissue can be accurately determined. In fluid dynamics, the FTP has also been used for studying free-surface water wave phenomena, which are caused by interaction mechanism between the underlying near-surface flow and external environment (Cobelli *et al*., 2009). In this study, a white liquid dye containing highly concentrated titanium oxide pigment paste was added into the water in a plexiglass container in order to enhance water's light diffusivity. The plane sinusoidal surface wave was generated by a paddle wave generator placed on one end of the container, while the vortex wave was created by a rotating disk placed at the bottom of the container.

In order to solve the inherent drawback of the FTP, high-frequency and zero-order components of the Fourier spectra were eliminated by using a quasi-sine projection and π-phase shifting technique (Li *et al*., 1990). In this method, the quasi-sine projection generated by defocusing a lens system removed high-frequency components, while the π-phase shifting removed the zero-order spectrum. However, although this technique can improve three times higher reconstructable slope, an error may occur due to an imperfect defocusing process. Therefore, the FTP technique was modified by employing the sinusoidal grating, instead of the quasi-sine projection (Yi and Huang, 1997). In this modified FTP, two sets of the grating images deformed by the object and the reference are required to eliminate the zero-order component. In the first set of the deformed images, the recordings are done by the grating pattern without the π-phase shifting. The π-phase shifted grating pattern is used for recording the second set of the deformed image. The zero-order spectrum is eliminated by subtracting the π-phase shifted the grating image from the one without the π-phase shifting. When the zero-order spectrum is removed, the modified method improves accuracy and measurement range. These improvements are traded-off for a slower response due to many grating projections. To overcome this problem, a windowed Fourier transform has been proposed (Kemao, 2004; Zhong and Weng, 2004). In this technique, the fundamental frequency information extracted by using a Gaussian-windowed Fourier transform. However, due to a stationary nature of the Gaussian window, which provides fixed spatially and frequency resolutions in the space-frequency domain, the frequency extraction cannot be optimized. Furthermore, the use of continuous wavelet transforms has been proposed to solve this problem. Unlike the windowed Fourier transform, the wavelet transform is a multi-resolution signal representation, which excels in non-stationary signal analysis. Although the Morlet wavelet (Zhong and Weng, 2005), the first-order derivative of a Gaussian function (DOG) (Gdeisat *et al*., 2006) and the Mexican hat wavelet (Li, Su, and Chen, 2009) have been used for eliminating the fundamental spectrum, how effective the use of the wavelet filter to eliminate the zero-order spectrum has never been rigorously studied. Consequently, their 3-D surface reconstruction performances are not well known.

1.2 Significance of the Study

This thesis studies the effectiveness of the elimination of the zero-order spectrum by using the three wavelet filters. Since this effect is related to the surface reconstruction, the 3-D reconstruction of the surface of isosceles triangular prisms will be experimentally conducted. The reason for using the triangular prism is that its slope, which determines the maximum range of the reconstruction, can be easily calculated. The study is done by evaluating the effects of the center frequency and the passband of the filters on the shape reconstructions. As a result, the most effective wavelet filter for the 3-D surface reconstruction can be determined.

1.3 Research Objectives

1.3.1 To study the effects of the center frequency and the width of the wavelet filter on the elimination of the zero-order spectrum.

1.3.2 To compare 3-D shape reconstruction performances of the FTP by using wavelet filters.

1.4 Scope and Limitation of the Study

1.4.1 The elimination of the zero-order spectrum and the reconstruction performances are experimentally studied.

1.4.2 The Morlet, the DOG and the Mexican hat wavelets are employed for eliminating the zero-order spectrum.

1.4.3 The test objects is isosceles prism with dimensions of 133.51 mm × 70.10 mm × 42.71 mm.

1.4.4 The reconstructed heights are compared with a direct contact measurement.

1.5 Organization of the Thesis

This thesis is organized as follows. In Chapter II, the principles of the FTP are reviewed. In Chapter III, the theory of wavelet transformation and its application to the filtering of the zero-order spectrum are discussed. In Chapter IV, experimental verifications of the FTP using the wavelet filtering are reported. Finally, the conclusion of this research work is presented in Chapter V.

CHAPTER II

FOURIER TRANSFORM PROFILOMETRY

This chapter reviews the theory of the FTP required to understand the discussion in this thesis. The review starts with a discussion of an optical setup for implementing the FTP. An extraction of the modulated phase information in the spatial frequency domain using Fourier transformation is then presented.

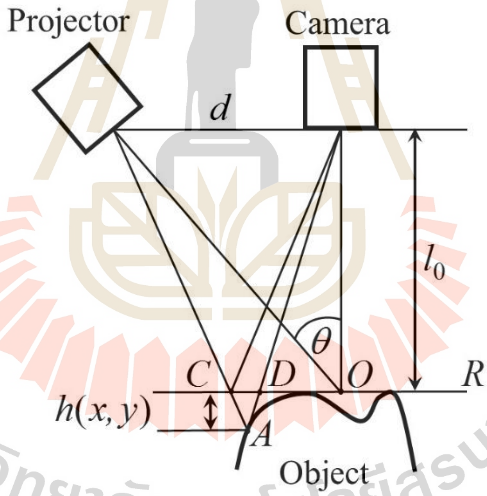

Figure 2.1 A crossed-optical geometry of the FTP.

Figure 2.1 shows the geometry of an optical setup for implementing the 3-D FTP. It consists of two functional parts. The first part is the grating projection system, which is implemented by using an LCD projector. The second one is the detection system with a CCD camera used to capture the grating deformed by the object being studied. The implementation is based on a crossed optical axes setup, in which their axes intersect in the reference plane R with the distance l_0 from the entrance pupil of the camera. The optical axes form a projection angle θ with the spatial separation d.

The camera records the grating patterns deformed by the object and the screen given by

$$g_1(x,y) = a(x,y) + ba(x,y)\cos[2\pi f_0 x + \phi(x,y)] \tag{2.1}$$

and

$$g_0(x,y) = r(x,y) + br(x,y)\cos[2\pi f_0 x + \phi_0(x,y)], \tag{2.2}$$

respectively. Here, $a(x,y)$ and $r(x,y)$ are irradiances by non-uniform light reflection caused by the object and by the screen, respectively. b is the modulation factor and f_0 is the fundamental frequency of the grating, which is inversely proportional to the grating pitch p_0 measured at the reference plane R. $\phi(x,y)$ is the phase distortion caused by the object, while $\phi_0(x,y)$ is the phase of the screen.

Figures 2.2(a) and (b) show the grating patterns deformed by the screen and the isosceles prism object, respectively. When the grating pattern is projected onto the 3-D surface, the grating pattern is deformed by the height profile. Owing to the angle formed by the camera and the projector, the deformed grating pattern has different frequency and intensity. The corresponding signals scanned at one row of the deformed gratings are shown in Figures 2.2(c) and (d), respectively.

For the sake of simplicity of the discussion, Eq. (2.1) can be rewritten as

$$g_1(x,y) = a(x,y) + c_1(x,y)\exp[j2\pi f_0 x] + c_1^*(x,y)\exp[-j2\pi f_0 x], \tag{2.3}$$

and Eq. (2.2)

$$g_0(x,y) = r(x,y) + c_0(x,y)\exp[j2\pi f_0 x] + c_0^*(x,y)\exp[-j2\pi f_0 x]\,, \tag{2.4}$$

where $c_1(x,y) = 0.5ba(x,y)\exp[j\phi(x,y)]$ and $c_0(x,y) = 0.5br(x,y)\exp[j\phi(x,y)]$.

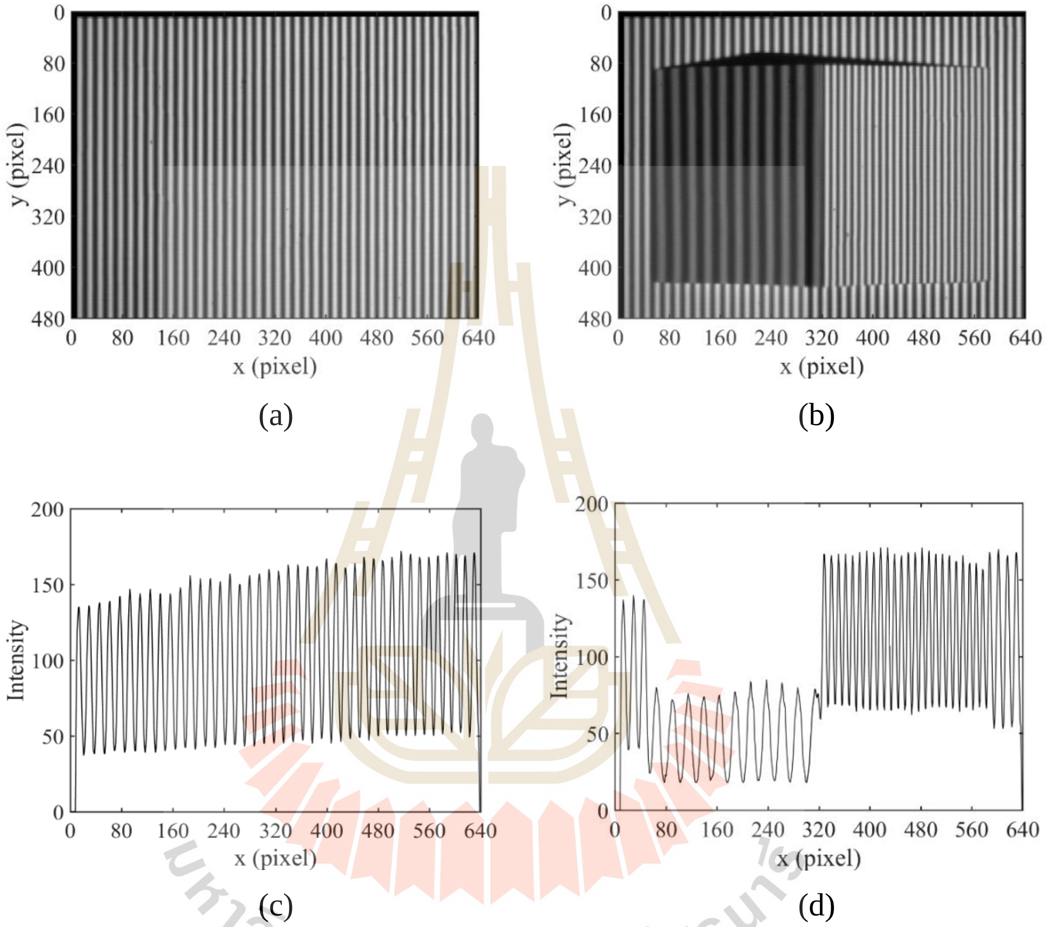

Figure 2.2 Grating patterns deformed by (a) the screen and (b) the object. Their corresponding signals scanned at the line 100th from the patterns in (c) Figure 2.2(a) and (d) Figure 2.2(b), respectively.

Fourier transform of a 1-D signal scanned from $g_1(x,y)$ and $g_0(x,y)$ are given by

$$G_1(f_x,y) = A(f_x,y) + C_1(f_x - f_0,y) + C_1^*(f_x + f_0,y)\,, \tag{2.5}$$

$$G_0(f_x,y) = R(f_x,y) + C_0(f_x - f_0,y) + C_0^*(f_x + f_0,y)\,, \tag{2.6}$$

where $A(f_x, y)$ and $R(f_x, y)$ describes the zero-order spectrum of non-uniform light reflection. $C(f_x - f_0, y)$ and $C^*(f_x + f_0, y)$ represent the fundamental frequencies which contain the phase information. As shown in Figure 2.3, they appear on the left and the right sides of the zero-order spectrum. Spectral distribution can be obtained from Eq. (2.1) and (2.2).

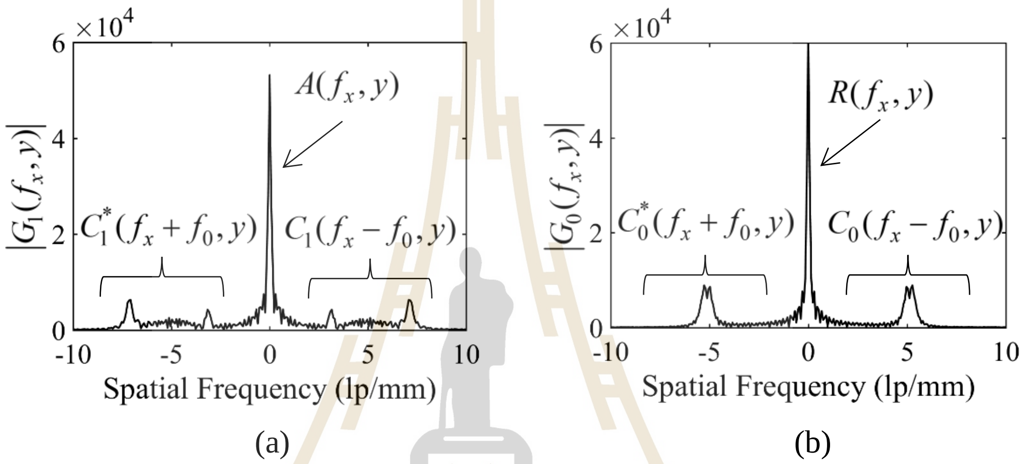

Figure 2.3 (a) Absolute values of the spectra $G_1(f_x, y)$ and (b) $G_0(f_x, y)$ of the 1D signals shown in Figures 2.2(c) and 2.2(d), respectively.

In order to extract the desired phase $\phi(x,y)$, the fundamental spectrum is selected by using a rectangular filter. By taking an inverse Fourier transform of the filtered fundamental spectrum, a new signal can be obtained from the grating patterns deformed by the object and the screen as

$$\hat{g}_1(x, y) = 0.5ba(x, y)\exp\{j[2\pi f_0 x + \phi(x, y)]\} \tag{2.7}$$

and

$$\hat{g}_0(x, y) = 0.5br(x, y)\exp\{j[2\pi f_0 x + \phi_0(x, y)]\}, \tag{2.8}$$

respectively. A complex logarithm of their product $\hat{g}_1 \cdot \hat{g}_0^*$ gives

$$\log[\hat{g}_1 \cdot \hat{g}_0^*] = \log[0.25b^2 a(x,y) r(x,y)] + j\Delta\phi(x,y)\,, \tag{2.9}$$

where $\Delta\phi(x,y) = \phi(x,y) - \phi_0(x,y)$ is the derived phase information. Since the phase calculated numerically by a computer has a range value from $-\pi$ to π, the phase needs to be unwrapped (Takeda, Ina, and Kobayashi, 1982). The height distribution are mathematically related to the derived phase $\Delta\phi(x,y)$ by (Takeda and Mutoh., 1983)

$$h(x,y) = \frac{l_0 \Delta\phi(x,y)}{\Delta\phi(x,y) - 2\pi f_0 d} \tag{2.10}$$

and the maximum reconstructed height is determined by

$$\left| \frac{\partial h(x,y)}{\partial x} \right|_{\max} < \frac{l_0}{3d}\,. \tag{2.11}$$

Since this is the maximum slope of the object profile that can be reconstructed by the conventional FTP, when the slope exceeds this limitation, the fundamental spectrum overlaps the zero-order and higher components, yielding wrong reconstruction.

CHAPTER III

WAVELET TRANSFORMATION

In this chapter, the theory of wavelet transform is reviewed. Three analyzing wavelets that are Morlet, the first-order derivative of Gaussian function (DOG) and the Mexican hat functions are discussed. Transfer functions of the three wavelets are derived to define their center frequencies and passbands.

3.1 Definition of wavelet transformation

Wavelet is a wave-like oscillation function which has a short duration. It is capable of providing simultaneously time and frequency information. Therefore, the wavelet can be employed to analyze non-stationary signals. The wavelet transforms of a signal pattern $g(x)$ is defined as (Watkins, 2012; Yan *et al.*, 2009)

$$W_g(s,\tau) = \frac{1}{\sqrt{s}} \int_{-\infty}^{\infty} w^* \left(\frac{x-\tau}{s} \right) g(x) dx , \tag{3.1}$$

where $w(x)$ is the continuous function in both space and frequency domains called the mother wavelet and $*$ stands for the complex conjugate. τ is the window shifting factor, while s is the scale factor.

The DOG wavelet generated from a Gaussian function $G = \exp\left(-(x)^2/2\sigma^2\right)$ is defined as (Gdeisat, Burton, and Lalor, 2006)

$$w_{G1}(x) = -\frac{x}{s^2\sigma_1^2} \exp\left(-\frac{(x/s)^2}{2\sigma_1^2} \right). \tag{3.2}$$

As for the Mexican hat wavelet, it is given by (Li, Su, and Chen, 2009)

$$w_{G2}(x) = -\frac{1}{s^2\sigma_2^2}\left(\frac{x^2}{s^2\sigma_2^2} - 1\right)\exp\left(-\frac{(x/s)^2}{2\sigma_2^2}\right), \tag{3.3}$$

while the Morlet wavelet is defined as (Zhong and Weng, 2005)

$$w_M(x) = \cos(2\pi f_c \frac{x}{s})\exp\left(-\frac{(x/s)^2}{2\sigma_3^2}\right). \tag{3.4}$$

Here, f_c is the center frequency of Morlet wavelet. σ_1^2, σ_2^2 and σ_3^2 are the variance of the wavelet functions in Eqs. (3.2), (3.3) and (3.4), respectively. Multiresolution analysis of the wavelet transform is done by changing the scale factor, yielding bandpass filters with different center frequencies and passbands.

In the frequency domain, the transfer functions of the DOG, the Mexican hat and the Morlet wavelet can be expressed as

$$W_{G1}(f_x) = 2\pi f_x s\sigma_1\sqrt{2\pi}\exp(-2\pi^2 f_x^2 s^2\sigma_1^2), \tag{3.5}$$

$$W_{G2}(f_x) = 4\pi^2 f_x{}^2 s\sigma_2\sqrt{2\pi}\exp(-2\pi^2 f_x^2 s^2\sigma_2^2), \tag{3.6}$$

and

$$W_M(f_x) = \frac{s\sigma_3}{2}\sqrt{2\pi}\left[\exp\left(-\frac{\left(2\pi f_x - \frac{2\pi f_c}{s}\right)^2 s^2\sigma_3^2}{2}\right)\right], \tag{3.7}$$

respectively. The center frequency of the wavelet filters can be determined from these transfer functions by setting their first derivatives equal to zero. Consequently, the center frequency of the DOG wavelet is equal to

$$f_{c1} = \frac{1}{2\pi s\sigma_1}, \tag{3.8}$$

while Mexican hat wavelet gives

$$f_{c2} = \frac{1}{\sqrt{2}\pi s \sigma_2}. \tag{3.9}$$

In the case of the Morlet wavelet, it's center frequency is

$$f_{c3} = \frac{f_c}{s}. \tag{3.10}$$

Figure 3.1(a) shows plots of the wavelet signals for the scale $s=1$. The solid, the dash-dot and the dash lines represent $w_{G1}(x)$, $w_{G2}(x)$ and $w_M(x)$, respectively. The corresponding transfer functions of the three wavelets are shown in Figure 3.1(b). They are plotted at the same center frequencies $f_{c1} = f_{c2} = f_{c3} = 9$ lp/mm. This frequency value is set by adjusting their variances to be $\sigma_1 = 0.01775$, $\sigma_2 = 0.025$ and $\sigma_3 = 0.07$, respectively.

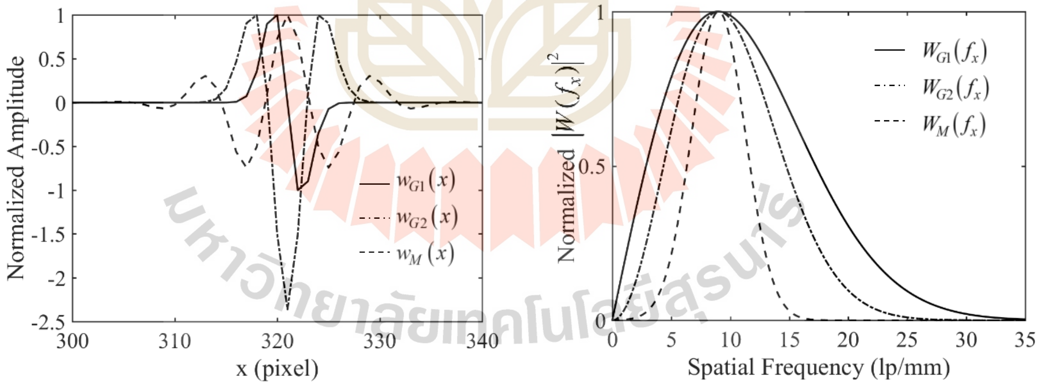

(a) (b)

Figure 3.1 (a) The wavelet signals $w_{G1}(x)$, $w_{G2}(x)$ and $w_M(x)$ for the scale $s=1$ and (b) their corresponding transfer functions.

In this study, the filter passband is defined as the width where the amplitude transfer function falls to e^{-2} times the maximum value. In the case of the DOG wavelet, the passband is given by

$$\Delta W_{G1} = \frac{0.40607}{s\sigma_1}\,. \tag{3.11}$$

The passband of the Mexican hat and the Morlet wavelets are found to be

$$\Delta W_{G2} = \frac{0.42619}{s\sigma_2} \tag{3.12}$$

and

$$\Delta W_{M} = \frac{2}{\pi s\sigma_3}\,, \tag{3.13}$$

respectively. It can be understood from Eqs. (3.8) - (3.13) that when the scale factor s is high, the filter has a low center frequency and narrow passband than the filter with a low scale.

It is obvious that the three wavelets have different responses in the space and the spectrum domains. Figure 3.1(b) reveals that firstly, besides having the broadest passband, the DOG wavelet starts linearly from the zero frequency. This low transition band may affect its effectiveness in the background elimination. Secondly, the Mexican hat wavelet has also broad passband with a quadratic response in both transition bands. Thirdly, in comparison with the others, the Morlet wavelet has a symmetrical transfer response and localized passband that is independent upon the center frequency.

3.2 Wavelet filtering in the FTP

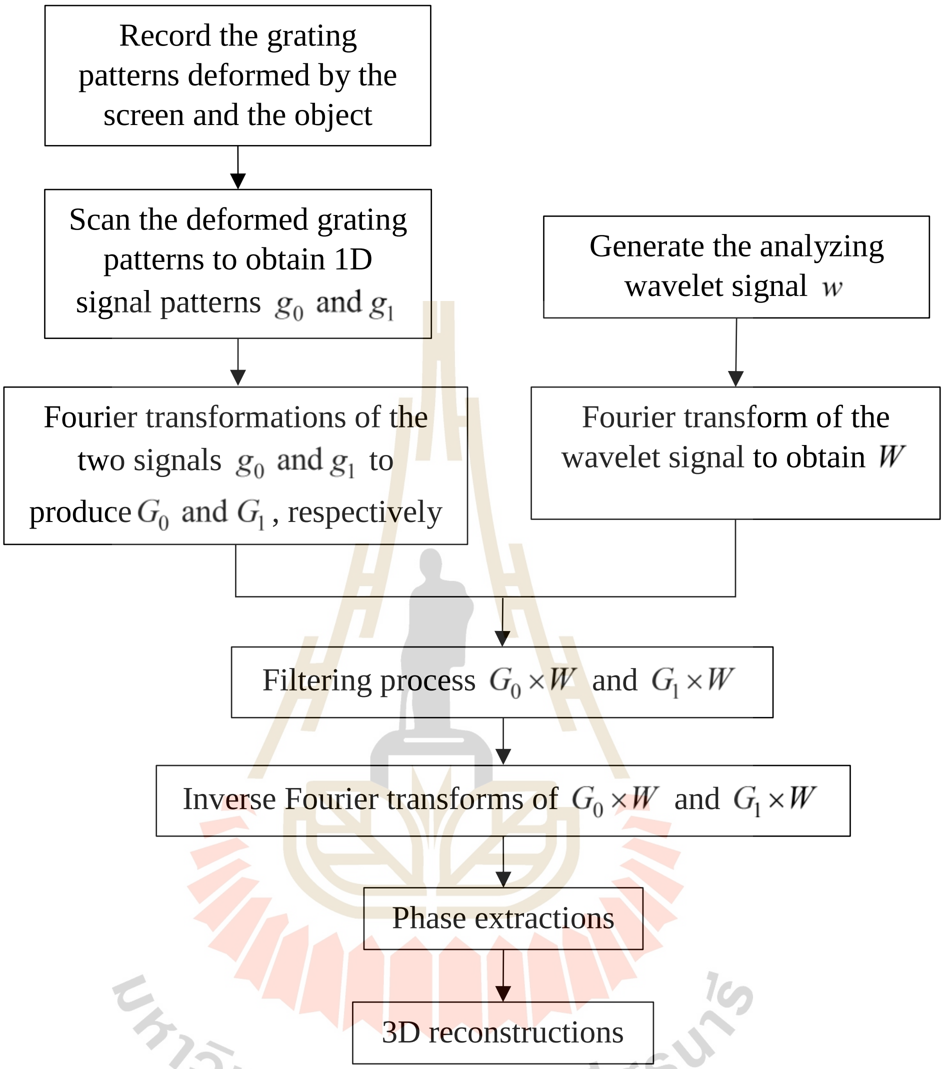

Figure 3.2 Diagram of flowchart in the FTP processing by using the wavelet filter.

Figure 3.2 shows a diagram of a flowchart to use wavelet filters in the FTP. First, the grating pattern images of the screen and the object are recorded. The 1D cross-sectional signals of the gratings deformed by the screen and the object are digitally scanned, yielding g_1 and g_0 of Eqs. (2.1) and (2.2), respectively. The two signals and the analyzing wavelet are then Fourier transformed, giving $G_1(f_x)$, $G_0(f_x)$ and

$W(f_x)$. The filtering of the fundamental spectra is done by multiplying $G_1(f_x)$, $G_0(f_x)$ by $W(f_x)$, respectively.

Figure 3.3 illustrates the filtering process of $G_1(f_x)$ by the Morlet wavelet $W_M(f_x)$. After the inverse Fourier transformation of the product, the desired phase extraction and the height reconstruction are performed by using the same step of the conventional FTP (Takeda and Mutoh., 1983).

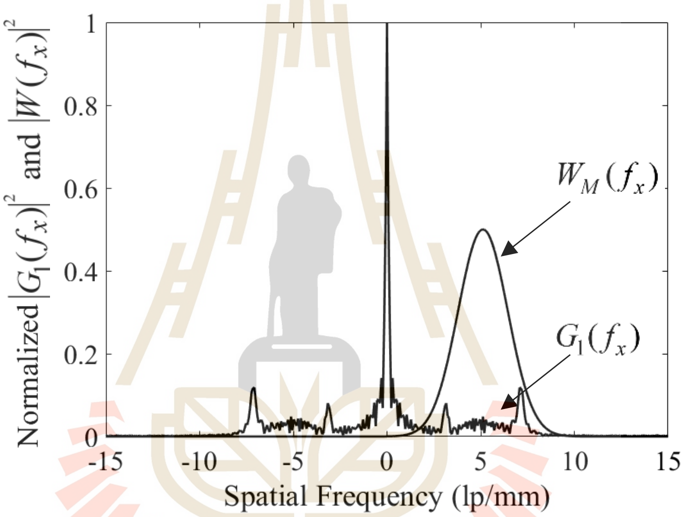

Figure 3.3 The fundamental spectrum filtering $G_1(f_x)$ by the Morlet wavelet filter $W_M(f_x)$.

CHAPTER IV

EXPERIMENTAL VERIFICATIONS

This chapter presents the experimental verifications of the FTP using the wavelet filters with the isosceles prisms as test objects. The effects of the center frequency and passband of the wavelet filter on the 3D shape reconstruction will be studied with respect to the pitch of the projected grating and the projection angle. In order to assess quantitatively the reconstruction performance, the FTP results are compared with those of the direct contact method.

4.1 Experimental Setup

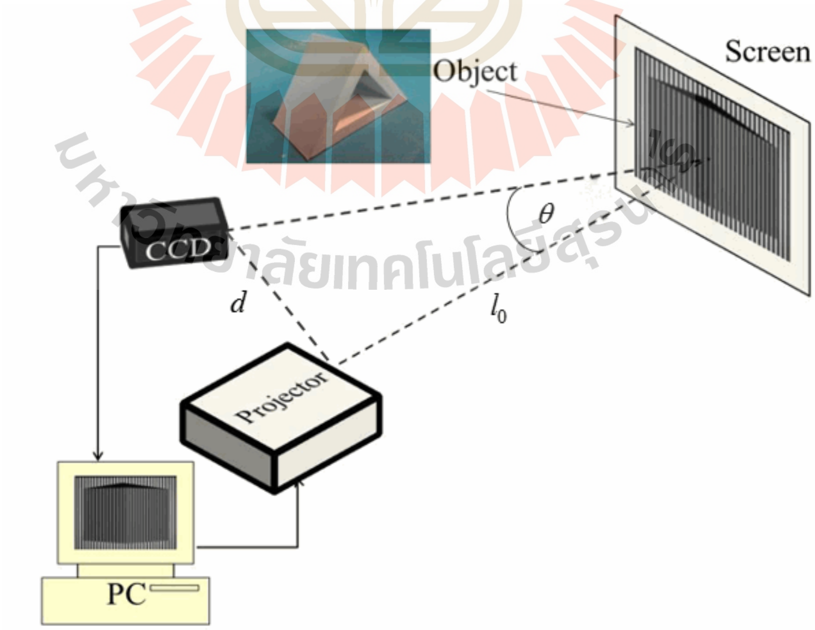

Figure 4.1 A schematic diagram of the FTP.

Figure 4.1 shows the schematic diagram of the optical setup for conducting this study. The grating pattern digitally generated by a computer system was projected onto the screen by using an LCD projector with a distance $l_0 = 1050$ mm away. The projected grating pattern on the screen was recorded by using a CCD camera whose axis makes the angle θ with respect to the projector axis. Two angles of projection in this study were 4° and 28° Consequently, the maximum measurable shape at these two angles was 0.62. After saving the recorded grating patterns, the desired phase information was numerically extracted for the shape reconstructions. The instrumentations used in this study are listed as follows:

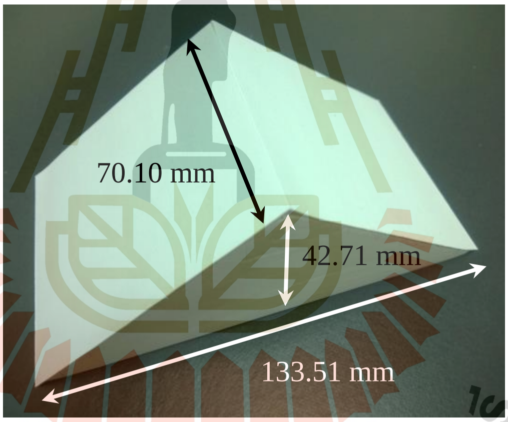

Figure 4.2 Isosceles prism with a slope of 0.64.

4.1.1 LCD projector (Toshiba, TLP-X2000) with resolution 1024×768 pixels.

4.1.2 CCD camera (Hamamatsu, C5948) with resolution 640×480 pixels and sensor area $8.3\ \text{mm} \times 6.3\ \text{mm}$.

4.1.3 Camera lens (AF Nikkor, f = 50 mm, f /1.4 D).

4.1.4 Digital height gauge (Moore and Wright, MW 190-30DBL), resolution 0.01 mm.

4.1.5 An isosceles prism object is shown in Figure 4.2 with the dimension of 133.51 mm × 70.1 mm × 42.71 mm and the slope 0.64.

4.1.6 MATLAB software version 2017a and Mathematica 10.

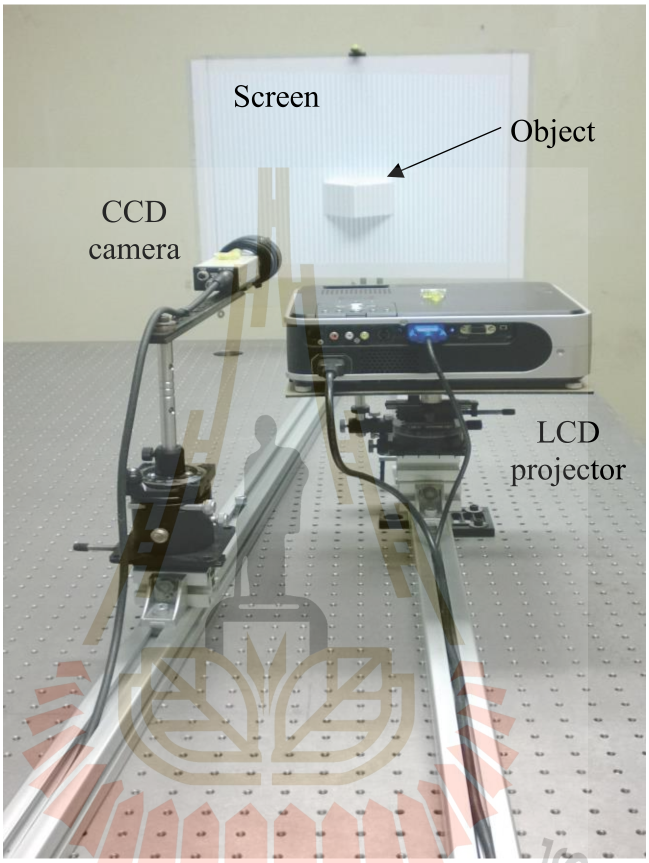

Figure 4.3 An optical setup of the FTP.

4.2 Calibration of the wavelet filters

The effectiveness of the wavelet filters for eliminating the zero-order spectrum was experimentally studied by using the optical setup shown in Figure 4.3. The sinusoidal gratings with the pitches p_0 of 4.84 mm and 3.24 mm were subsequently projected onto the screen at the two angles. The deformed grating images $g_0(x, y)$ were saved into tiff format. Figures 4.4(a) and (b) show the grating pattern with the pitch of

4.84 mm deformed by the screen at the projection angle $\theta = 4^\circ$ and its fundamental spectrum, respectively. In this study, the peak of the fundamental spectrum was used to determine the center frequency of the corresponding wavelet filters.

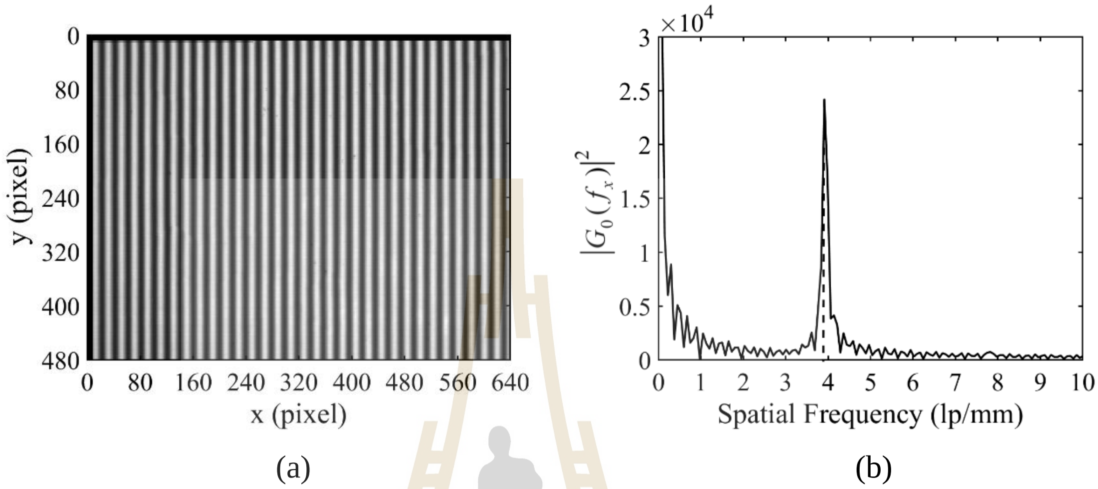

Figure 4.4 (a) Image of the grating pattern with the pitch p_0 = 4.84 mm deformed by the screen and (b) its fundamental spectrum.

Table 4.1 Center frequencies of the grating pattern deformed by the screen with respect to the projection angles $\theta = 4^\circ$ and 28°.

	Center frequency f_c (lp/mm)	
Angle θ (°)	p_0 = 4.84 mm	p_0 = 3.24 mm
4	3.916	5.798
28	3.464	5.120

Table 4.1 summarizes the center frequencies of the deformed gratings with the different pitches $p_0 = 4.84$ and 3.24 mm at different angles of projection $\theta = 4^\circ$ and 28°. It is clear that for the same grating pitch, the bigger projection angle causes the lower the center frequency.

4.2.1 The effect of the center frequency

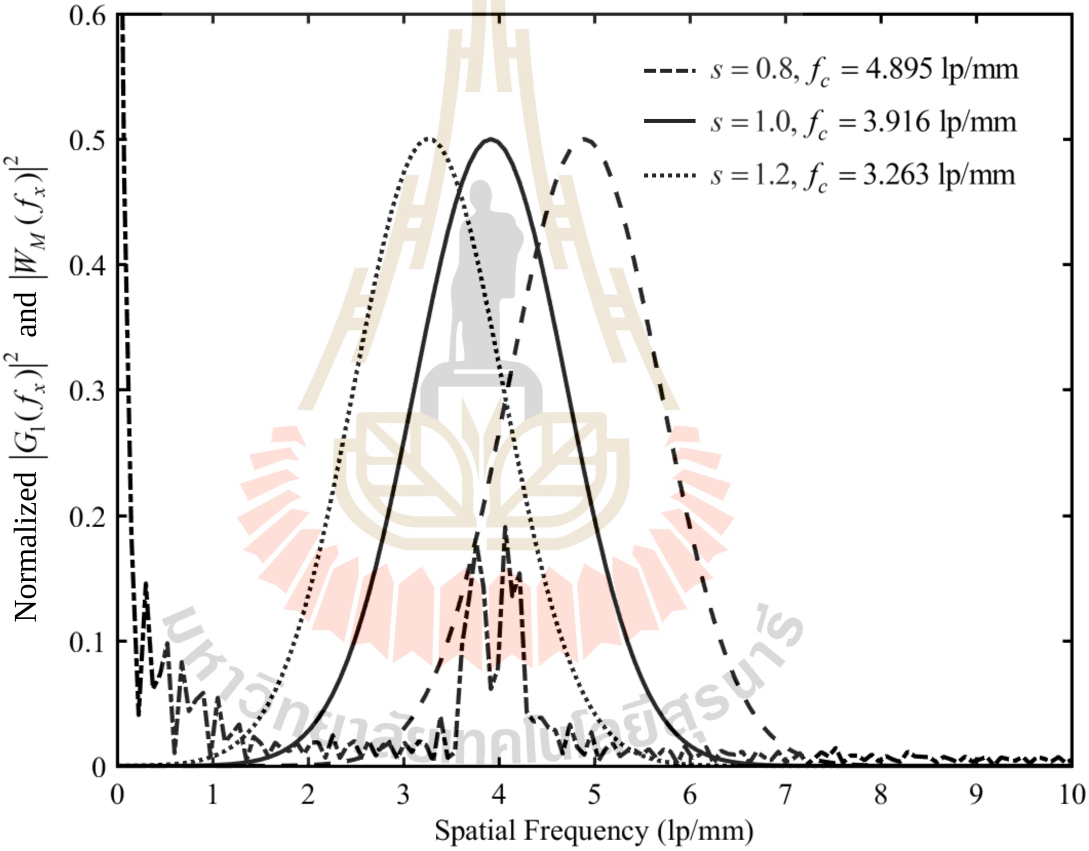

Figure 4.5 Effects of the scale factor s on the center frequency of the Morlet wavelet filter.

In this study, the center frequency of the mother wavelet filters was set to be equal to the center frequency of the deformed grating to be analyzed, while the scale factor s was set to be unity. According to the multiresolution property of the wavelet transform, the scale factor can be finely adjusted in order to have an accurate center frequency.

Figure 4.5 shows the effects of the scale factor on the center frequency of the Morlet wavelet filter. The dash-dotted line represents the spectrum of the grating pattern with the pitch $p_0 = 4.84$ mm, which was deformed by the isosceles object at the angle $\theta = 4°$. The center frequency of the mother wavelet was $f_c = 3.916$ lp/mm. The solid line represents the transfer functions of the wavelet filter with the scale $s = 1$ and the variance $\sigma_3 = 0.20$. The dashed line is for the transfer function with the scale $s = 0.8$ and the variance $\sigma_3 = 0.25$, while the dotted line is for the scale $s = 1.2$ and the variance $\sigma_3 = 0.17$. In order to study the effect of the center frequency, the passband of the three filters are set to be equal. According to Eq. (3.11), this is achieved by defining different variance value for each wavelet filter. The center frequency of filters will be lowered when the scale becomes higher.

Figure 4.6 shows the effect of the center frequency on the shape reconstruction of the prism. It is obvious that when the center frequency of the wavelet filter is lower than that of the fundamental spectrum, high-frequency components of the fundamental spectrum are discarded and high-frequency components of the zero-order spectrum are included by the wavelet filter. As a result the reconstructed peak is distorted and the two sides have a curved surface. The left vertex is rounded, while the right one fluctuates. In the case of higher center frequency, the reconstructed shape is also degraded. This is caused by the fact that unwanted high-frequency components greater than that of the fundamental spectrum are included by the wavelet filter, while low-frequency components of the fundamental spectrum are discarded. This causes fluctuations of the left vertex and smoothing on the right one. Thus, only when the center frequency of the filter matches to that of the fundamental spectrum that is the scale factor s =1, the 3-D shape reconstruction can be optimized.

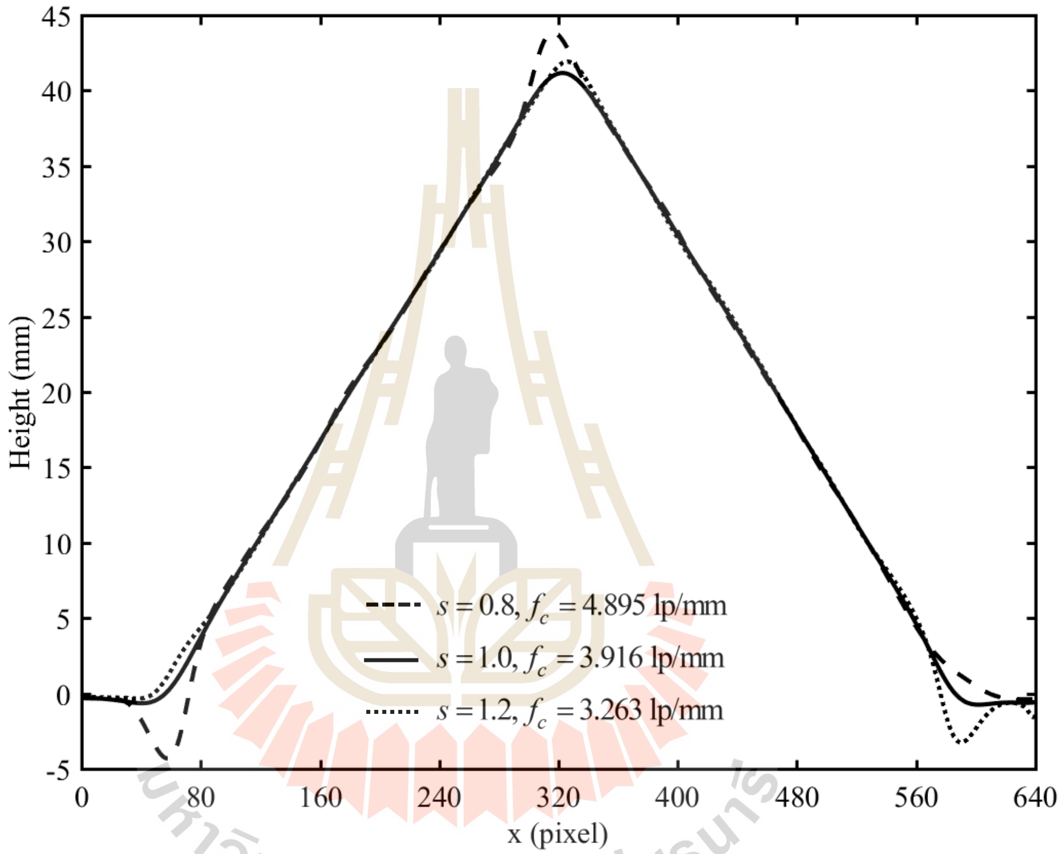

Figure 4.6 Reconstructed prism profiles by using the Morlet wavelet filters with the center frequency defined in Figure 4.5.

4.2.2 The effect of the filter passband

Figures 4.7 shows the effects of varying the variance σ_3 on the passband of Morlet wavelet for the scale s =1. The dotted, the solid and the dashed lines represent the filter passbands with ΔW_M = 4.90 lp/mm, 3.18 lp/mm and 2.36 lp/mm corresponding to the variances of σ_3 = 0.13, 0.20 and 0.27, respectively. The dash-dotted line represents the same spectrum of the deformed grating pattern shown in Figure 4.5. According to Eq. (3.13), the passband becomes narrow when the variance σ_3 has a large value. The effects of the passband on the shape reconstructions can be seen in Figure 4.8.

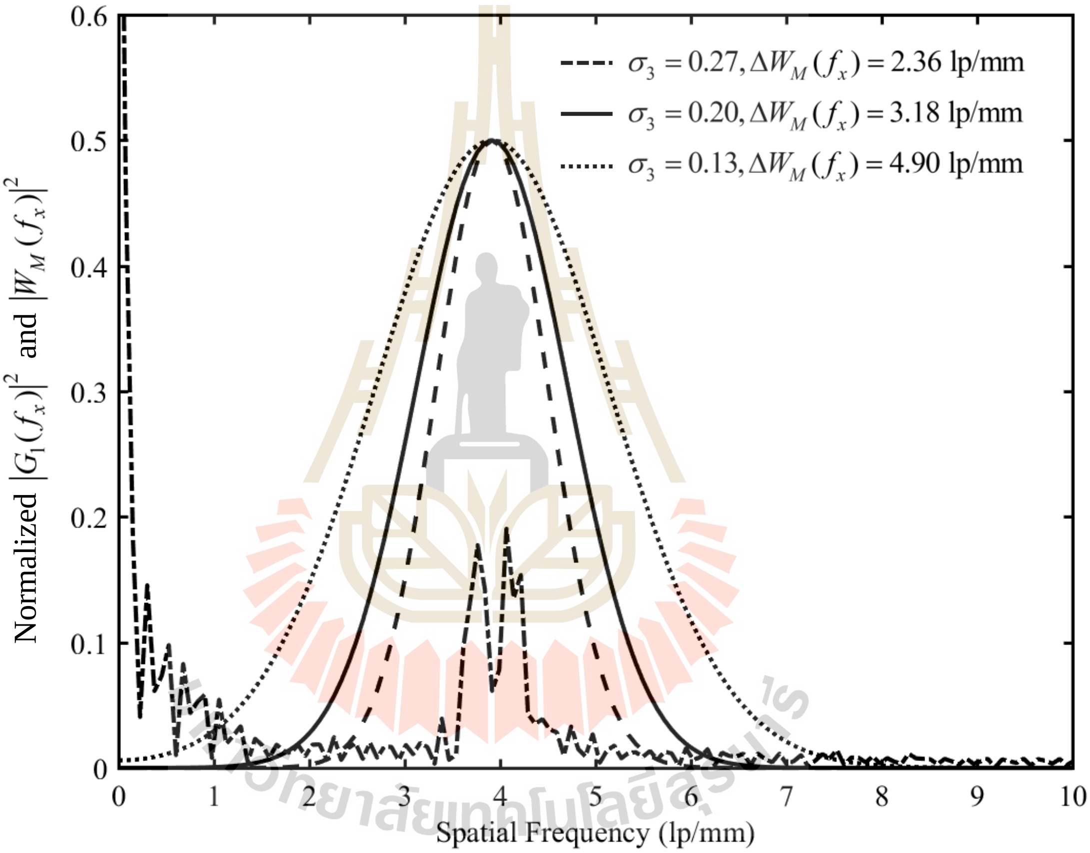

Figure 4.7 Effects of the variance σ_3 on the Morlet wavelet filter passband $\Delta W_M(f_x)$.

When the passband of the Morlet wavelet filter is either broader or narrower than the fundamental spectrum undesired, low and high-frequency components of the grating deformed by the object are included in the reconstruction process. Consequently, the wrong reconstruction is obtained such as the degradations of the peak, the vertex and the side surfaces are high. Since the spectral width of the fundamental spectrum cannot be exactly defined, the filter passband and its center frequency are very important factors for the 3-D shape reconstruction. Note that in the case of the DOG and the Mexican hat wavelets, the filter passband depends on the center frequency of the filter. When the center frequency is low, the filter passband is narrow. While it is broad when the center frequency is high.

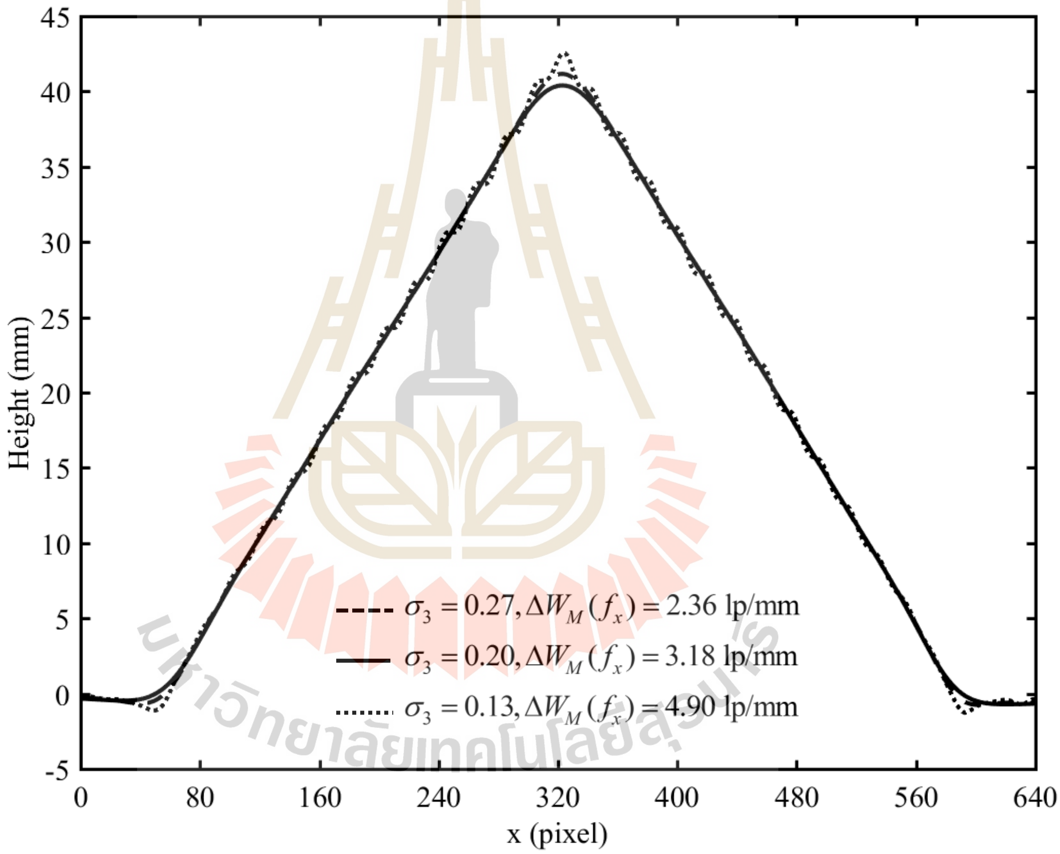

Figure 4.8 Reconstructed prism profiles by using the Morlet wavelet filters with the passband defined in Figure 4.7.

4.3 Experimental results

4.3.1 Shape reconstructions of the prism object

4.3.1.1 Small projection angle

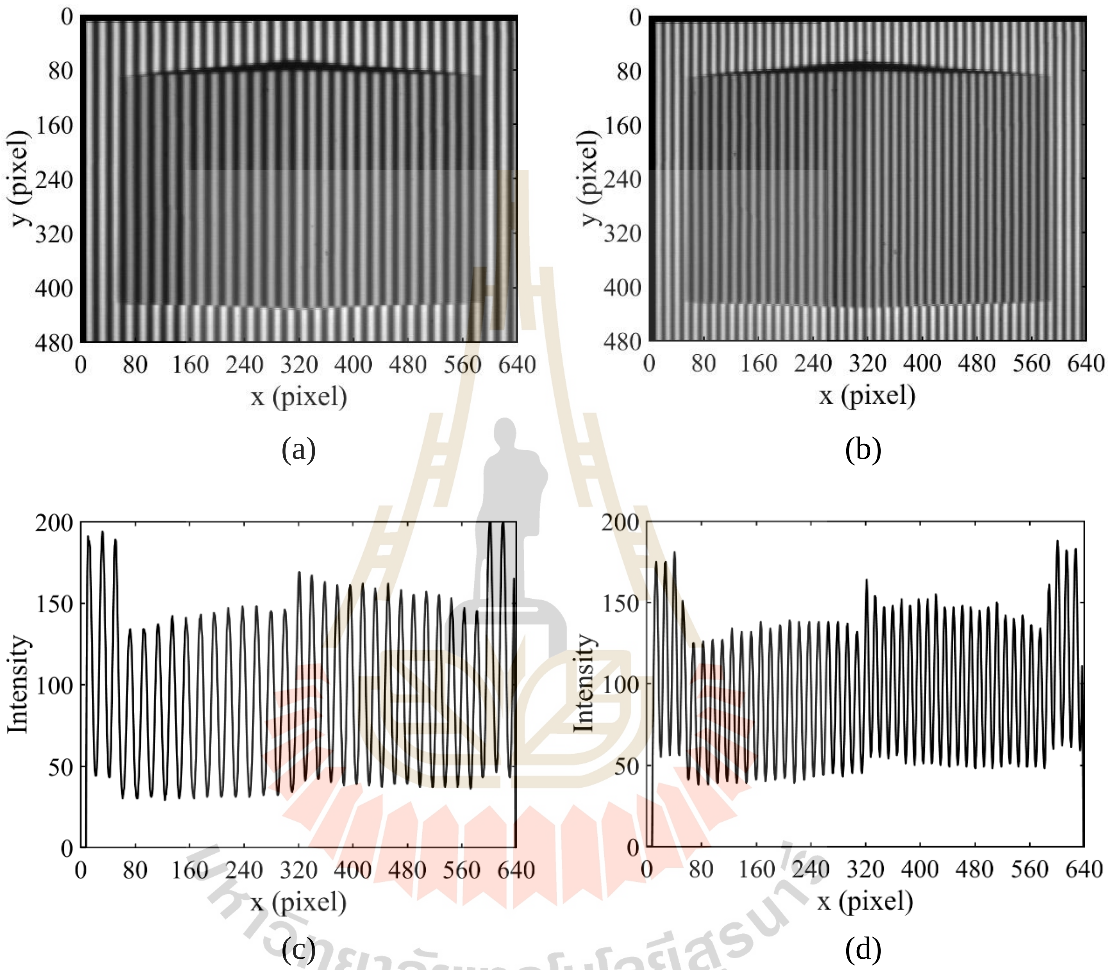

Figure 4.9 Grating patterns deformed by the prism object in situation that the projected gratings have of the pitch of (a) 4.84 mm and (b) 3.24 mm at the angle $\theta = 4^{\circ}$. Intensities scanned at the 240th row of (c) Figure (a) and (d) Figure (b), respectively.

Figure 4.9 shows the grating patterns deformed by the prism object at the angle projection $\theta = 4^{\circ}$. In Figure 4.9(a), the projected grating pattern has the pitch

$p_0 = 4.84$ mm, while the pitch in Figure 4.9(b) is 3.24 mm. The corresponding 1-D cross-sectional intensities scanned at the 240th row are shown in Figures 4.12(c) and (d), respectively. It can be observed that the grating pattern incident on the left side of the prism is elongated, while the one on the right side is compressed. The intensity on the prism left side is lower than the right side. This is because of the difference of the optical path length from the camera to the two prism sides. The longer the path length, the lower the light intensity due to the broader area. It is clear also that the higher the grating frequency, the lower the intensity of the deformed grating.

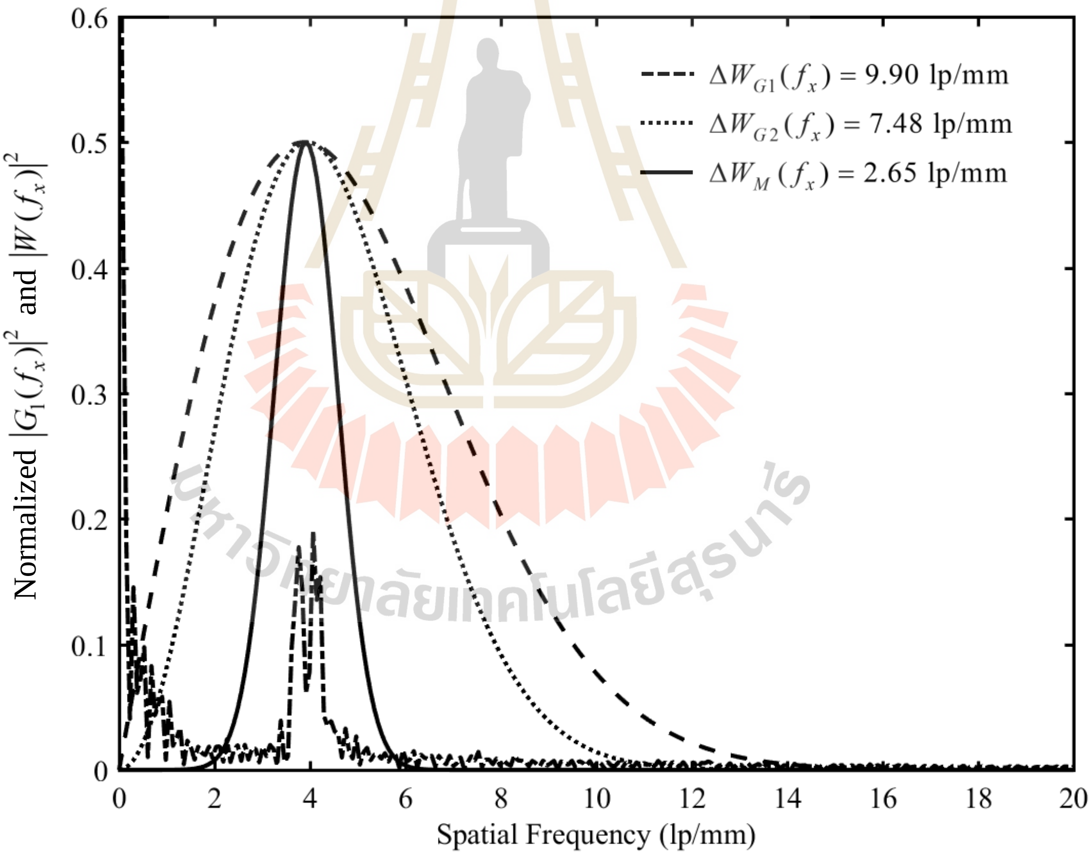

Figure 4.10 Filtering of the fundamental spectrum of the grating pattern (p_0 =4.84 mm) deformed by the prism at the angle $\theta = 4^\circ$ via $W_{G1}(f_x)$, $W_{G2}(f_x)$ and $W_M(f_x)$.

Figure 4.10 illustrates the fundamental spectrum filtering for the background elimination and the surface reconstruction by using the wavelet filters in the situation that the projected grating has the pitch p_0 =4.84 mm. The dashed, the dotted, and the solid lines represent the filters $W_{G1}(f_x)$, $W_{G2}(f_x)$ and $W_M(f_x)$, respectively. They have the same center frequency of 3.916 lp/mm, while their passbands are 9.90 lp/mm, 7.48 lp/mm and 2.65 lp/mm, respectively.

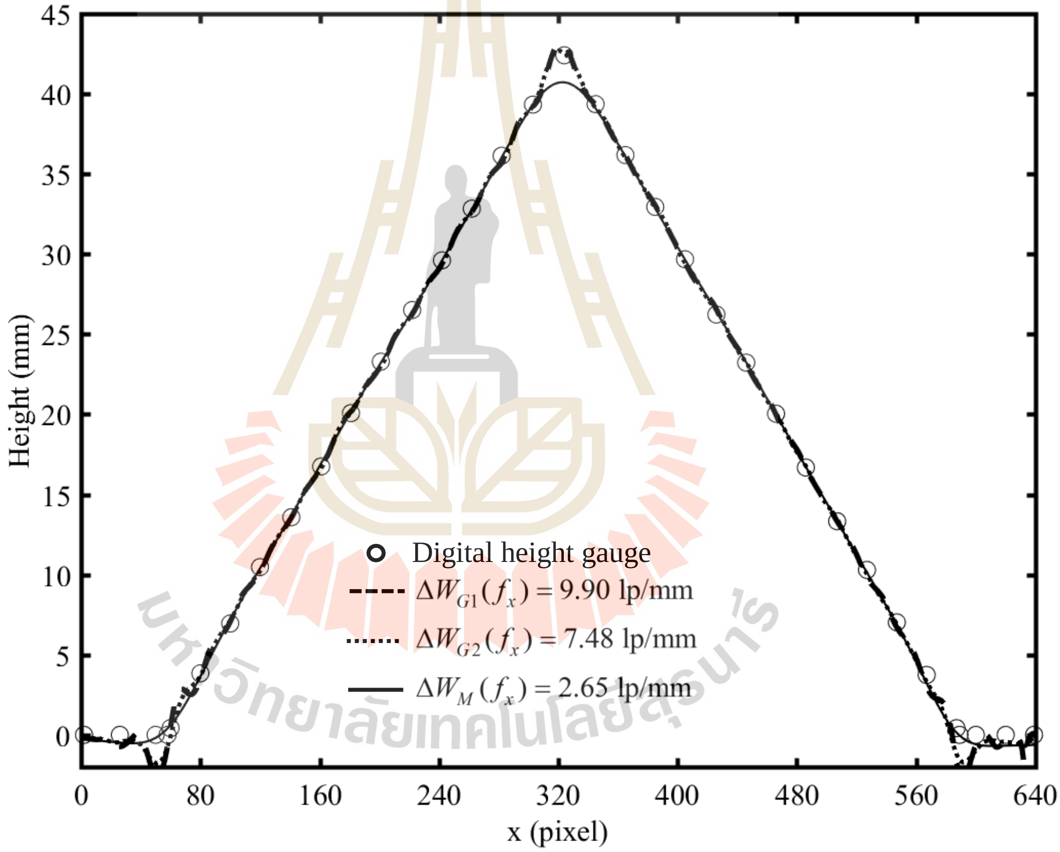

Figure 4.11 Reconstructed of prism profiles from the deformed grating (p_0 =4.84 mm) at the angle $\theta = 4^\circ$ via $W_{G1}(f_x)$, $W_{G2}(f_x)$ and $W_M(f_x)$.

Figure 4.11 shows the prism profiles reconstructed by using the three wavelet filters compared with the direct contact measurement. The dashed, the dotted and the solid lines represent the reconstructions by using $W_{G1}(f_x)$, $W_{G2}(f_x)$ and $W_M(f_x)$, respectively. The results show that although the reconstructed peak has the wrong height, the Morlet wavelet $W_M(f_x)$ can reconstruct the prism and the reference plane surfaces smoother than the others. This is because its narrow passband discards high-frequency components of the prism.

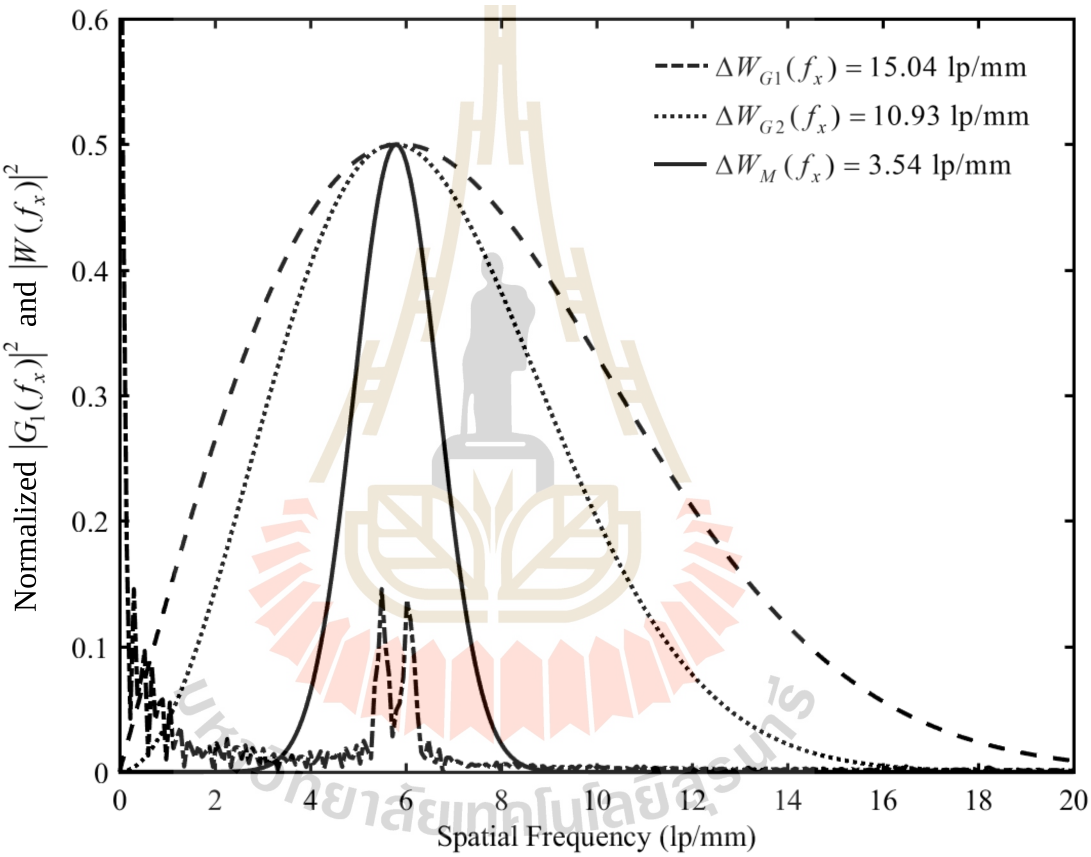

Figure 4.12 Filtering of the fundamental spectrum of the grating pattern (p_0 =3.24 mm) deformed by the prism at the angle $\theta = 4^\circ$ via $W_{G1}(f_x)$, $W_{G2}(f_x)$ and $W_M(f_x)$.

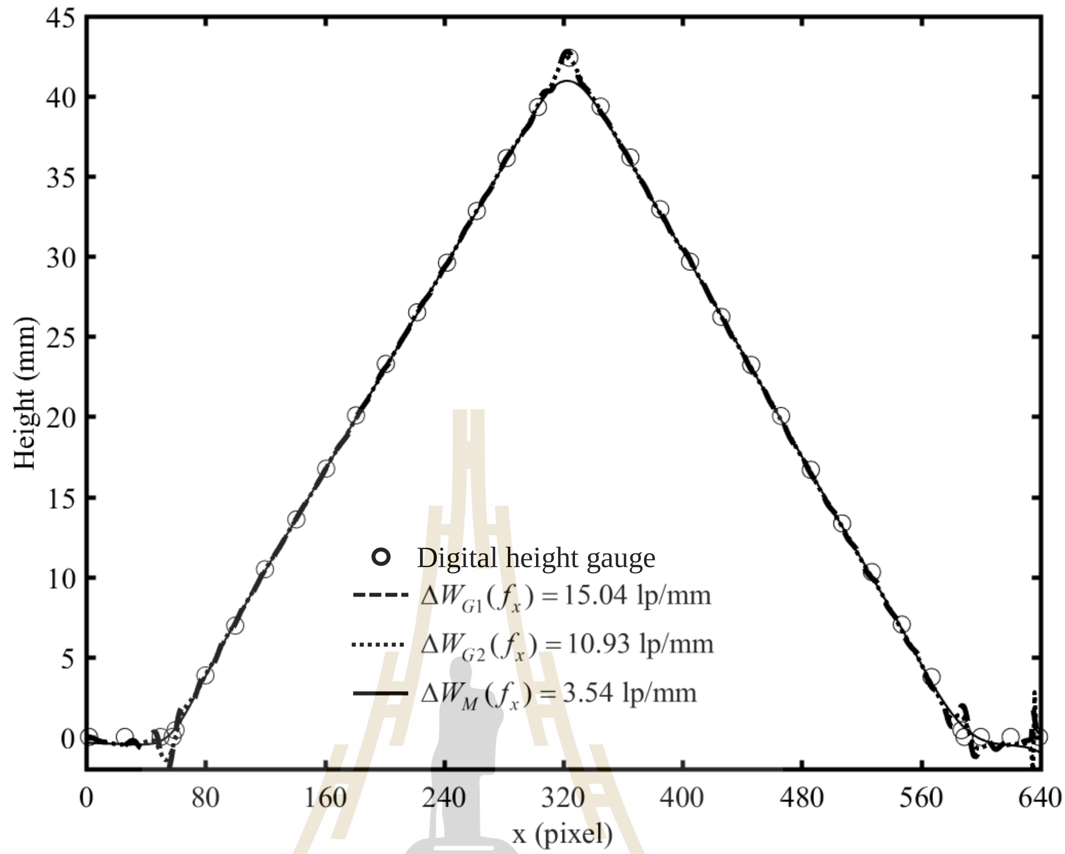

Figure 4.13 Reconstructed prism profiles from the deformed grating (p_0 =3.24 mm) at the angle $\theta = 4^{\circ}$ via $W_{G1}(f_x)$, $W_{G2}(f_x)$ and $W_M(f_x)$.

The effective filtering of the fundamental spectrum by using the wavelet filters in the situation that the projected grating has the pitch $p_0 = 3.24$ mm is illustrated in Figure 4.12. The dashed, the dotted and the solid lines represent the $W_{G1}(f_x)$, $W_{G2}(f_x)$ and $W_M(f_x)$ having the passbands of 15.04 lp/mm, 10.93 lp/mm and 3.54 lp/mm, respectively. According to Table 4.1, the center frequency of the fundamental frequency is 5.798 lp/mm. Therefore, the separation of the fundamental and the zero-order spectra is bigger than that of Figure 4.10. Since the center frequency of the wavelet filters must be equal to that of the fundamental spectrum, their passbands broaden. The result of filtering higher components of the zero-order spectrum corrupts the fundamental spectrum.

Figure 4.13 shows the prism profiles reconstructed by using the three wavelet filters compared with the direct contact method. It is apparent that when the fundamental and the zero-order spectra are well separated, the two sides of the prism can be smoothly reconstructed. However, since the broader passbands of the filters $W_{G1}(f_x)$ and $W_{G2}(f_x)$ include high-frequency components of the zero-order spectrum, the right surfaces around the vertex and the base could not be correctly reconstructed.

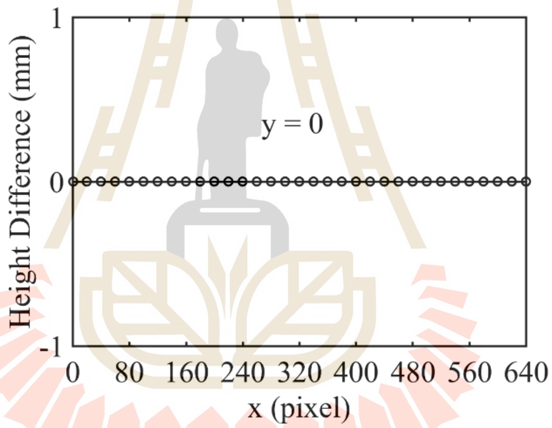

Figure 4.14 The ideal reconstruction of height differences.

In order to compare the reconstruction performances of the three wavelets, the differences between the heights measured by the direct contact method and the wavelet-based FTPs are calculated. Figure 4.14 shows a distribution of ideal height differences represented by the circle symbols for all points of measurement. In this error-free height reconstruction, the relation between the height difference in the *y*-axis and the position in the *x*-axis can be mathematically expressed by using a linear equation $y = 0$ represented by the dashed line. This is valid because the height difference is equal to zero. In the case of non error-free reconstructions, the relationship is given by $y = ax+b$, where a represents the distribution of the height differences and b corresponds to the average value of the differences for a is much smaller than unity. The linear equation of the height difference distribution can be calculated by using the linear regression (Douglas *et al*., 2012).

$$a = \sum_{i=1}^{n}(x_i - \overline{x})(y_i - \overline{y}) \Big/ \sum_{i=1}^{n}(x_i - \overline{x})^2 , \tag{4.1}$$

where x_i is i^{th} the position of the difference in the x-axis, $\overline{x}$ is the mean of x_i. y_i is the value of the i^{th} difference in the y-axis and $\overline{y}$ is the mean of y_i. The value of the factor a may be zero, positive or negative. When the factor a is equal to zero, the prism reconstruction has symmetrical height differences with respect to the peak position. The positive a means the height differences on the left side of the reconstructed prism profile has a lower value than those on the right side. In the case of the negative value, the right differences are higher than those on the left side. This implies that the smaller the factor a and b, the better the height profile reconstruction.

Figures 15(a), (b) and (c) show comparisons of the height differences shown in Figures 4.11 and 4.13 by using the wavelet filters $W_{G1}(f_x)$, $W_{G2}(f_x)$ and $W_M(f_x)$ for different center frequencies, respectively. In general, the wavelet filters having the high center frequencies have lower reconstruction performance than those with the lower ones. This is because although the spectral separation between the zero-order and the fundamental spectra is wider, the corresponding filter passband becomes broader. Consequently, the spectral leaking from the zero-order spectrum and the unwanted high-frequency components corrupt the fundamental spectrum. In the case of the DOG wavelet, the passband is the broadest, therefore, its reconstruction performance is the lowest. The Mexican hat can reconstruct the sharpest prism peak among others. In contrast, although its peak reconstruction has a high error, the Morlet wavelet has the lowest average of the height differences, regardless of the center frequency values.

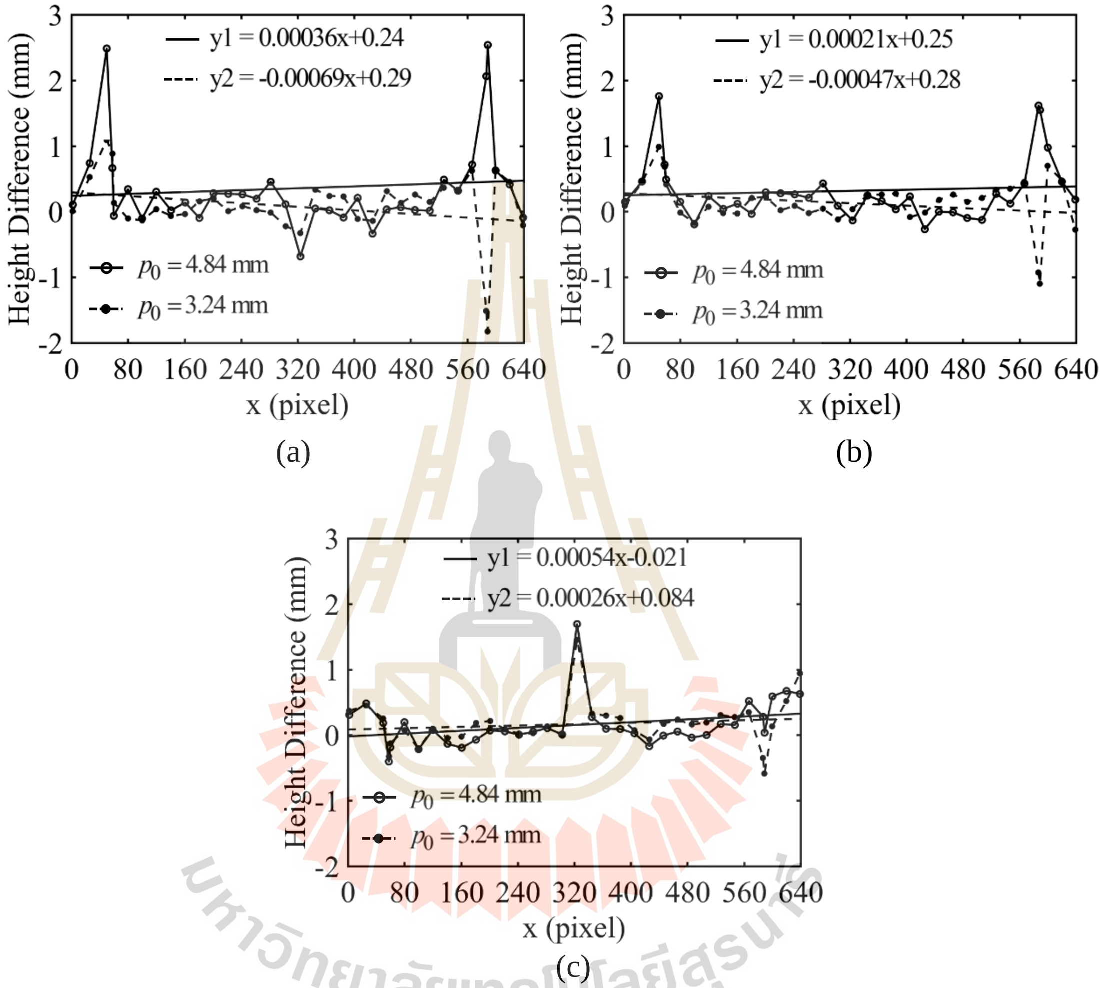

Figure 4.15 Comparisons of the height differences of the reconstructed prism at the angle $\theta = 4°$ for different center frequencies of (a) $W_{G1}(f_x)$, (b) $W_{G2}(f_x)$ and (c) $W_M(f_x)$, respectively.

Table 4.2 summaries the reconstructed performance of the three wavelets at the small projection angle as a function of the center frequency. The wavelet DOG and the Mexican hat are good in the reconstruction of the prism peak due to the broad passbands, while the Morlet wavelet has the lowest error because it could reconstruct the vertex and the prism side better than the others.

4.3.1.2 Large projection angle

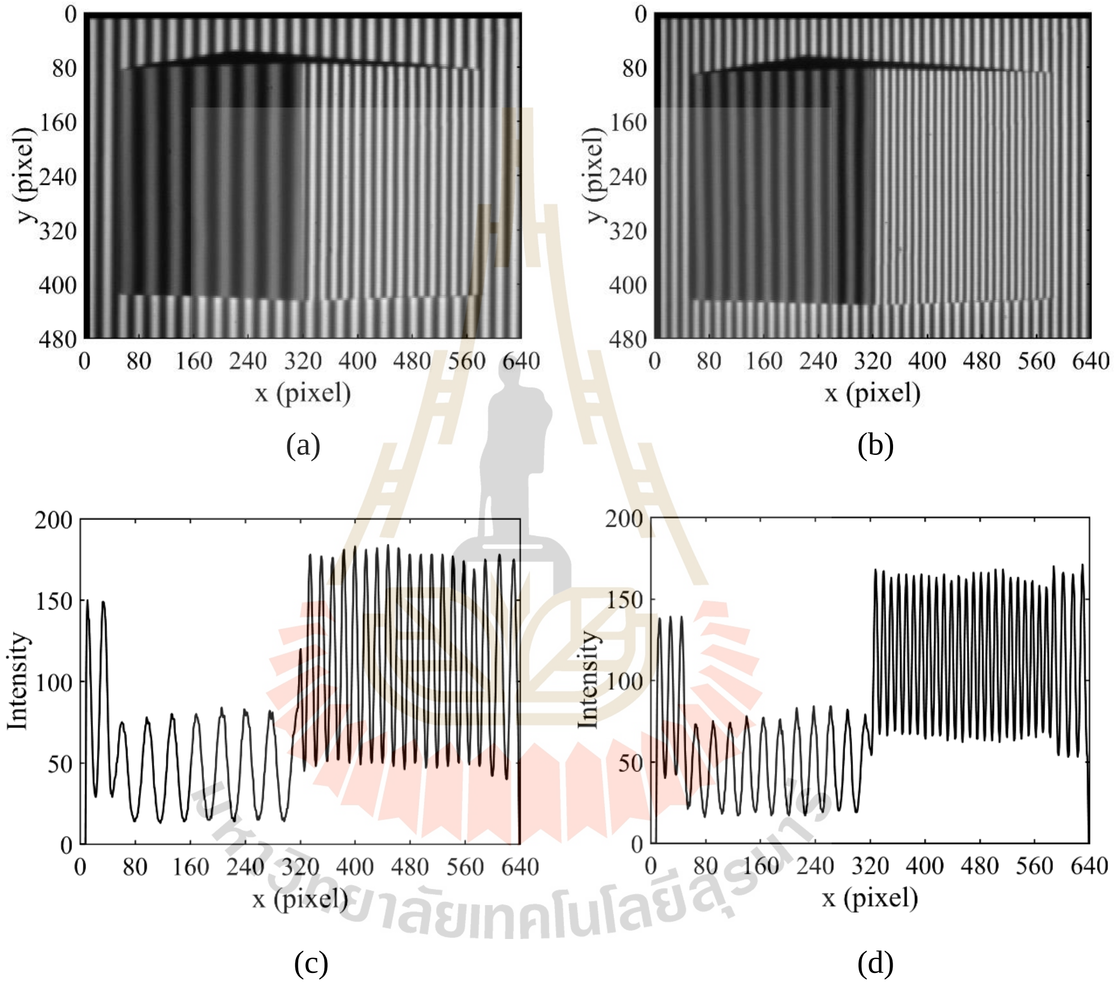

Figure 4.16 Grating patterns deformed by the prism object in situation that the projected gratings have the pitch of (a) 4.84 mm and (b) 3.24 mm at the angle $\theta = 28^{\circ}$. Intensities scanned at the 240th row of (c) Figure (a) and (d) Figure (b), respectively.

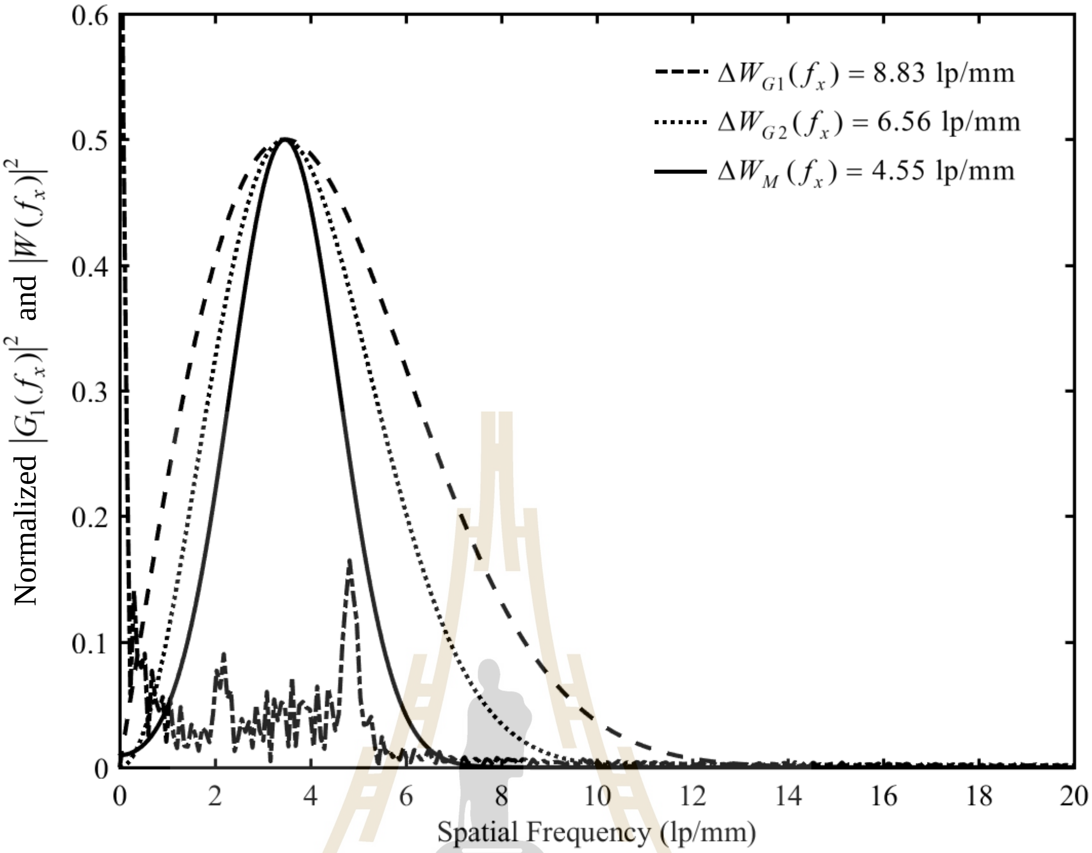

Figure 4.17 Filtering of the fundamental spectrum of the grating pattern (p_0 =4.84 mm) deformed by the prism at the angle $\theta = 28^\circ$ by using $W_{G1}(f_x)$, $W_{G2}(f_x)$ and $W_M(f_x)$.

Figures 4.16(a) and (b) show the grating patterns p_0 =4.84 mm and 3.24 mm, deformed by the prism at the projection angle $\theta = 28^\circ$, respectively. Their 1-D cross-sectional intensities scanned at the 240$^{\text{th}}$ row are plotted in Figures 4.16(c) and (d), respectively. In comparison with Figure 4.9, it is clear that the pitch of the deformed grating pattern on the left and the right sides are obviously different, because of the significant difference between the optical path lengths from the projector to the two sides of the prism object. Therefore, the fundamental spectrum of the deformed grating pattern is broader than that caused by the smaller projection angle. Consequently, its center frequency becomes lower.

This can be observed from Figure 4.17, which illustrates the spectrum filtering by the three wavelet filters. In this figure, the projected grating had the pitch $p_0 = 4.84$ mm. Each filter is represented by the same type of line described in Figure 4.9. The passbands of $W_{G1}(f_x)$, $W_{G2}(f_x)$ and $W_M(f_x)$ are 8.83 lp/mm, 6.56 lp/mm and 4.55 lp/mm, respectively, with the same center frequency of 3.464 lp/mm. Since the center frequency of the wavelet filters reduces their corresponding passbands become narrow.

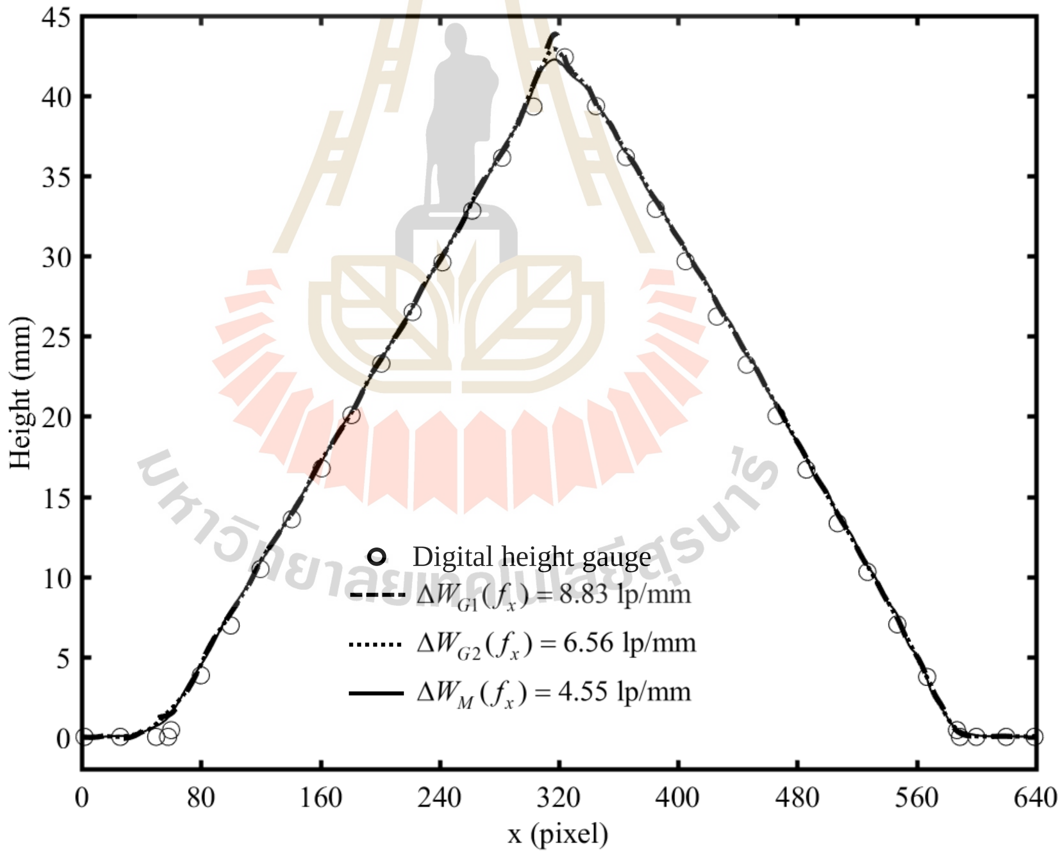

Figure 4.18 Reconstructed prism profiles from the deformed grating (p_0 =4.84 mm) at the angle $\theta = 28^\circ$ via $W_{G1}(f_x)$, $W_{G2}(f_x)$ and $W_M(f_x)$.

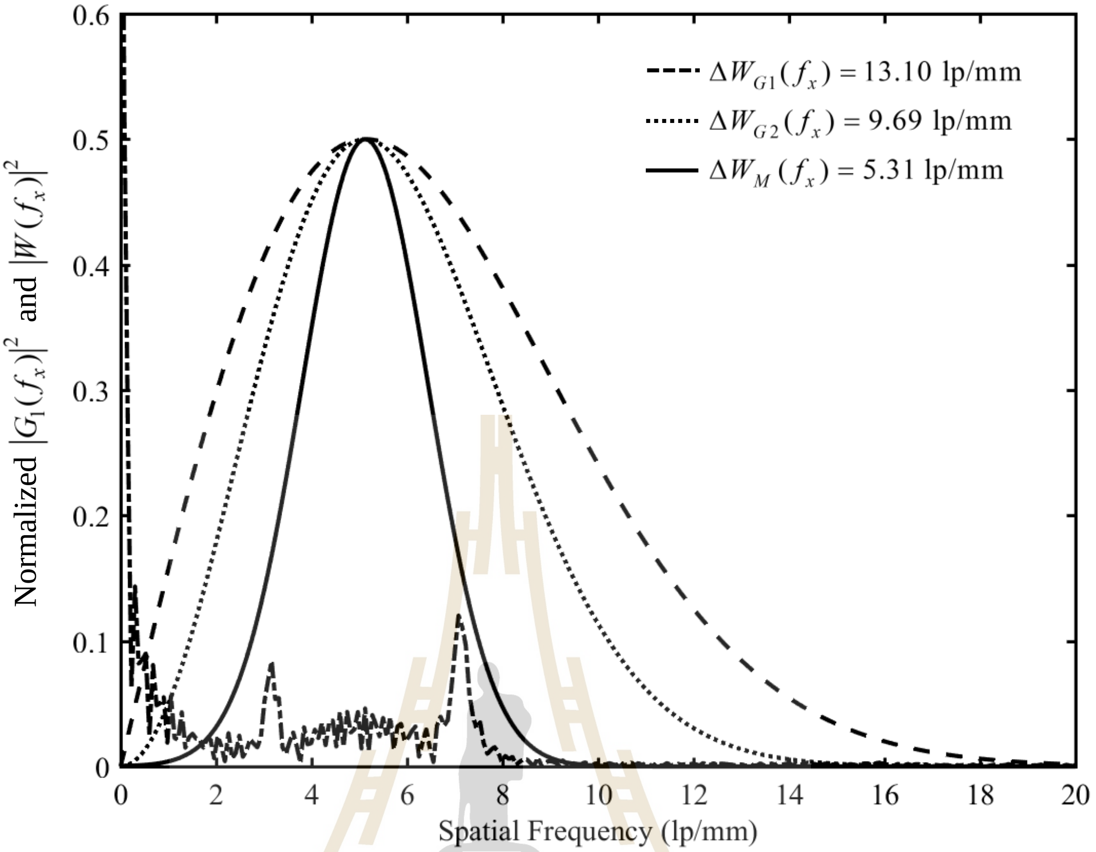

Figure 4.19 Filtering of the fundamental spectrum of the grating pattern (p_0 =3.24 mm) deformed by the prism at the angle $\theta = 28^\circ$ by using $W_{G1}(f_x)$, $W_{G2}(f_x)$ and $W_M(f_x)$.

Figure 4.18 shows the reconstructed prism profiles from the deformed grating pattern p_0 =4.84 mm at the projection angle $\theta = 28^\circ$ by using the wavelet filters. The dashed, the dotted and the solid lines represent the filters $W_{G1}(f_x)$, $W_{G2}(f_x)$ and $W_M(f_x)$ having the passbands of 8.83 lp/mm, 6.56 lp/mm and 4.55 lp/mm. Owing to the low center frequency, most high-frequency components of the fundamental spectrum are discarded and more unwanted zero-order spectrum components are included in the filtering. As a results the prism profiles reconstructed by using the three filters have asymmetrical shape, curved side surface, non-zero base and wrong peak heights.

Figure 4.19 shows the filtering of the fundamental of the grating pattern (p_0 =3.24 mm) deformed by the prism at the angle $\theta = 28^\circ$ by using the three wavelet filters. The dashed, the dotted and the solid lines represent the $W_{G1}(f_x)$, $W_{G2}(f_x)$ and $W_M(f_x)$, whose passbands are 13.10 lp/mm, 9.69 lp/mm and 5.31 lp/mm, respectively. They have the same center frequency of 5.120 lp/mm. Since the fundamental spectrum has a high center frequency, broadening of its spectral width may be less affected by the zero-order spectrum.

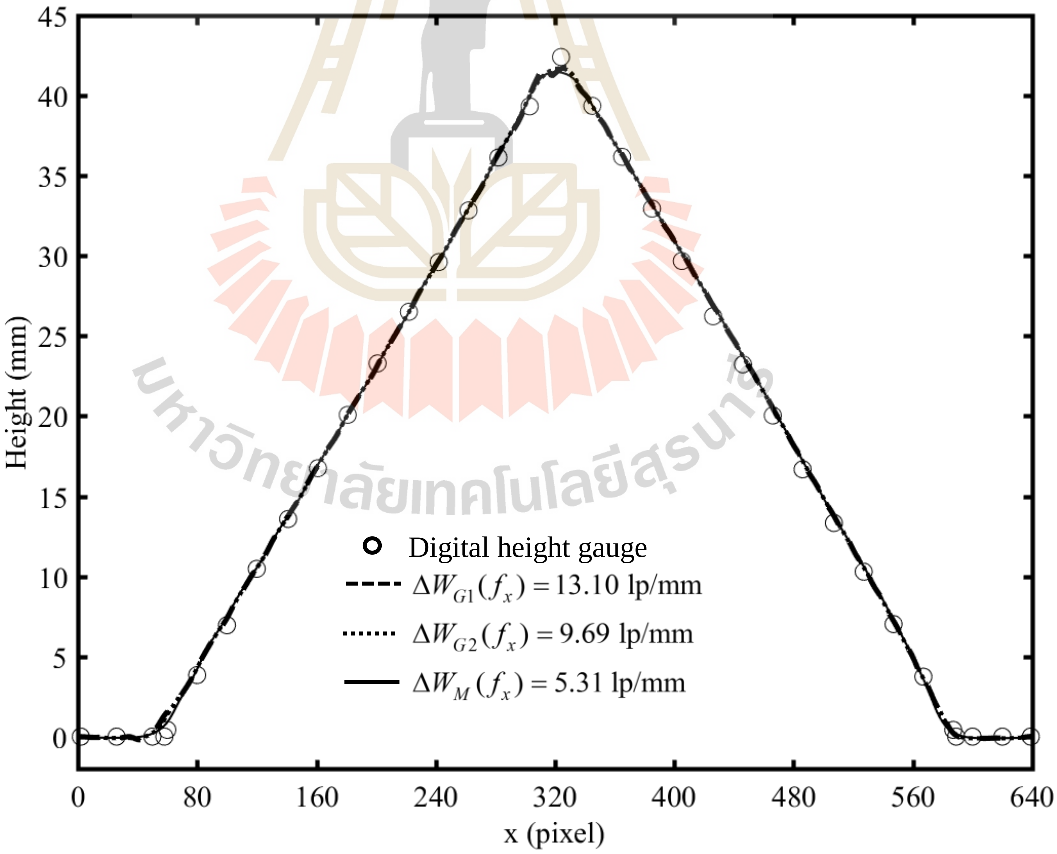

Figure 4.20 Reconstructed prism profiles from the deformed grating (p_0 =3.24 mm) at the angle $\theta = 28^\circ$ via $W_{G1}(f_x)$, $W_{G2}(f_x)$ and $W_M(f_x)$.

Figure 4.20 shows the reconstructed prism profiles by using the wavelet filters. The surfaces of the left and right sides prism are smooth and their reconstructed heights are in better agreement with the direct contact measurement. However, the base near the two vertices and the peak height cannot be correctly reconstructed. These may be caused by the fact that the wavelets $W_{G1}(f_x)$ and $W_{G2}(f_x)$ include not only the zero-order spectrum components, but also the unwanted high-frequency components.

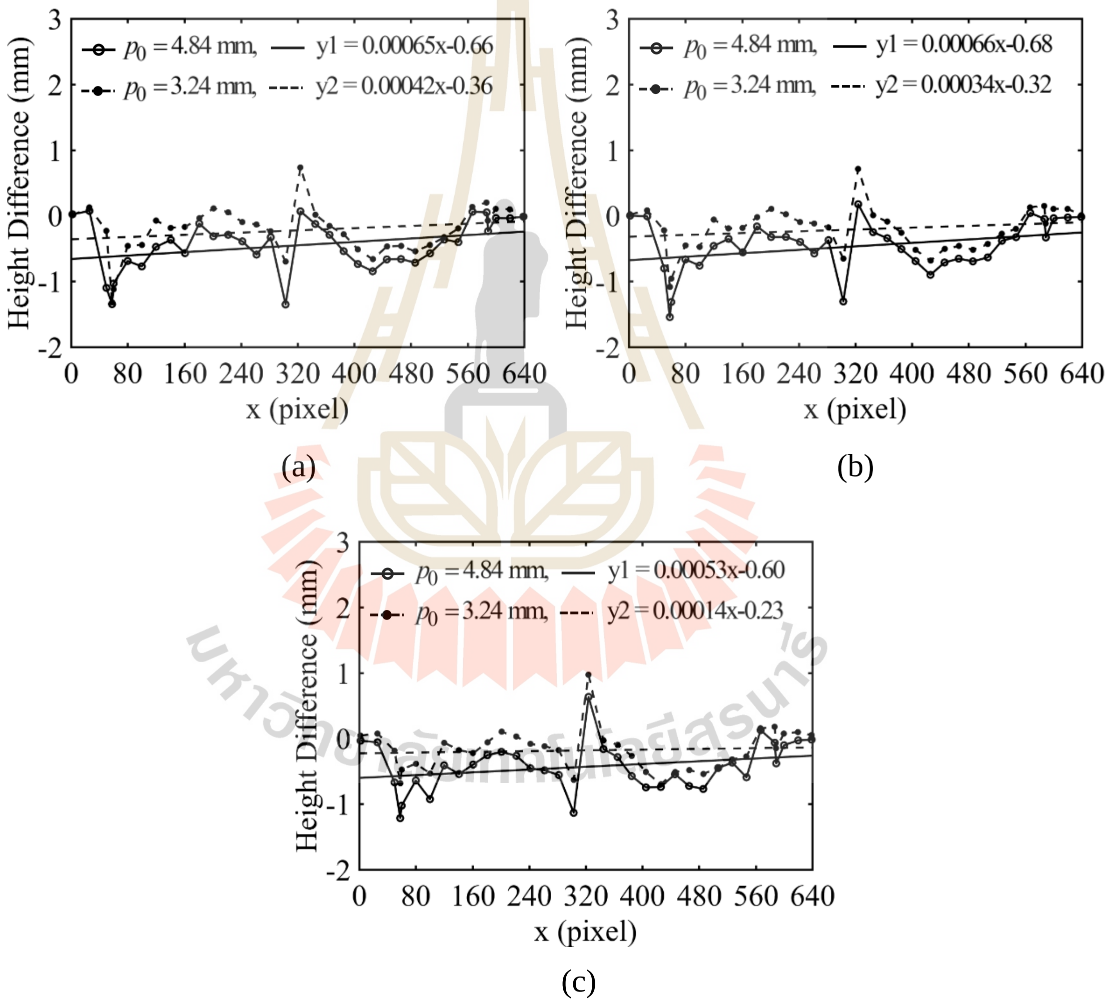

Figure 4.21 Comparisons of the height differences of the reconstructed prism at the angle θ= 28° for different center frequencies of (a) $W_{G1}(f_x)$, (b) $W_{G2}(f_x)$ and (c) $W_M(f_x)$, respectively.

Figures 4.21(a), (b) and (c) show the height differences produced by the FTP reconstructions at the big projection angle using the three wavelets with different center frequencies. It is clear that the average of the height differences is higher than that obtained by the small angle. This is because the big projection angle broadens the fundamental spectrum. When the center frequency of the deformed grating is low, the broaden fundamental spectrum overlaps with the zero-order spectrum. The summary of the reconstruction performance of the three wavelet filters is presented in Table 4.3. Regardless of the shapes of the peak, the vertex and the prism side, it is apparent that the Morlet wavelet has the lowest average of the height differences.

In summary, the experimental results show that the wavelet filters can be used for the FTP reconstruction from the deformed grating patterns with a small pitch that are recorded at the small projection angle. When the spectral leak from the zero-order and the unwanted high-frequency spectra are included in the prism shape reconstructions, the right and the left vertices fluctuates, respectively. These spectral inclusions produce also curved prism sides. The DOG wavelet has the poorest performance on the prism shape reconstructions, while the Mexican hat wavelet is good in the peak reconstruction. This is because, unlike the DOG wavelet which has a linear response in the low transition band, the Mexican hat has broad passband with a quadratic response in both transition bands. Finally, owing to its well localized passband and independency upon the center frequency, the Morlet wavelet has the lowest errors in the height measurements among other.

Table 4.2 Reconstruction performances of the three wavelet filters at the small projection angle.

$\theta = 4°$												
Grating	Peak			Vertices			Sides			Average of Errors		
f_c	$W_{G1}(f_x)$	$W_{G2}(f_x)$	$W_M(f_x)$	$W_{G1}(f_x)$	$W_{G2}(f_x)$	$W_M(f_x)$	$W_{G1}(f_x)$	$W_{G2}(f_x)$	$W_M(f_x)$	$W_{G1}(f_x)$	$W_{G2}(f_x)$	$W_M(f_x)$
Low	Rounded	Rounded	Rounded	Fluctuate	Fluctuate	Rounded	Curved	Curved	Less curved	Small	Small	Smallest
High	Less rounded	Sharp	Rounded	Fluctuate	Fluctuate	Rounded	Curved	Curved	Less curved	Small	Small	Smaller

Table 4.3 Reconstruction performances of the three wavelet filters at the big projection angle.

$\theta = 28°$												
Grating	Peak			Vertices			Sides			Average of Errors		
f_c	$W_{G1}(f_x)$	$W_{G2}(f_x)$	$W_M(f_x)$	$W_{G1}(f_x)$	$W_{G2}(f_x)$	$W_M(f_x)$	$W_{G1}(f_x)$	$W_{G2}(f_x)$	$W_M(f_x)$	$W_{G1}(f_x)$	$W_{G2}(f_x)$	$W_M(f_x)$
Low	Distorted	Distorted	Distorted	Fluctuate	Fluctuate	Rounded	Curved	Curved	Less curved	Small	Small	Smallest
High	Distorted	Distorted	Distorted	Less fluctuate	Less fluctuate	Rounded	Less curved	Less curved	Less curved	Small	Small	Smaller

CHAPTER V

CONCLUSIONS

The 3-D shape reconstructions using the wavelet-based FTP have been experimentally studied. In the study, the isosceles prism was used as the object, while the DOG, the Mexican hat and the Morlet wavelet filters were used to extract the phase information from the fundamental spectrum by eliminating the unwanted background of the deformed grating patterns. The study took into account the effects of the grating pitch and the projection angle.

To study the reconstruction performance of the wavelet-based FTP, the transfer function of the three wavelets were mathematically derived. The derivation results reveal that firstly, the passband of the mother wavelets is determined by the signal width of the variance in the space domain. Secondly, unlike the DOG and the Mexican hat wavelets, the center frequency and the passband of the Morlet wavelet are independent to each other. Thirdly, the Morlet wavelet has the most-localized passband, while that of the DOG wavelet is the broadest. Fourthly, the low transition band of the DOG wavelet has a linear frequency response. Hence, the effect of the spectral leak from the zero-order spectrum is the strongest. Furthermore, the spectral width of the fundamental spectrum is not only dependent upon the object height but also on the projection angle such that the bigger the projection angle, the broader the fundamental spectrum and the lower the center frequency. For this reason, the transfer function of the wavelet filter is designed by defining its center frequency to be equal to the center frequency and the grating patterns deformed by the screen.

The experimental reconstructions of the isosceles prism object show that the wavelet filters can be used for the FTP reconstruction from the deformed grating patterns, provided that the fundamental and the zero-order spectra are separated. To satisfy these conditions the grating pitch must be small and the deformed grating patterns are generated at the small projection angle. The Mexican hat wavelet can reconstruct sharp prism peak, while the Morlet wavelet has the lowest average error in the height measurements. The reasons for these are that the Mexican hat wavelet has a broad passband with a quadratic response in both transition bands. In the case of the Morlet wavelet, it has well localized passband, which can be independently defined without affecting its center frequency.

REFERENCES

REFERENCES

Cobelli, P. J., Maurel, A., Pagneux, V., and Petitjeans, P. (2009). Global measurement of water waves by Fourier transform profilometry. **Exp. Fluids** 46(6): 1037-1047.

Douglas, C. M., Elizabeth, A. P., and G. Geoffrey, V. (2012). Introduction to Linear Regression Analysis. 5th ed. New Jersey, Canada: John Wiley & Sons, Inc.

Gdeisat, M. A., Burton, D. R., and Lalor, M. J. (2006). Eliminating the zero spectrum in Fourier transform profilometry using a two-dimensional continuous wavelet transform. **Opt. Commun.** 266(2): 482-489.

Guo, X., Liu, X., Wang, X., Tian, F., Liu, F., Zhang, B., Hu, G., and Bai, J. (2010). A Combined Fluorescence and Microcomputed Tomography System for Small Animal Imaging. **IEEE Trans. Biomed. Eng.** 57(12): 2876-2883.

Kemao, Q. (2004). Windowed Fourier transform for fringe pattern analysis. **Appl. Opt.** 43(13): 2695-2702.

Lalos, J., Mrak, M., Pavlovcic, U., and Jezersek, M. (2015). Handheld optical system for skin topography measurement using fourier transform profilometry. **J. Mech. Eng.** 61(5): 285-291.

Li, J., Su, X., and Guo, L. (1990). Improved Fourier transform profilometry for the automatic measurement of three-dimensional object shapes**, Opt. Eng.** 29 (12): 1439-1444.

Li, S., Su, X., and Chen, W. (2009). Spatial carrier fringe pattern phase demodulation by use of a two-dimensional real wavelet. **Appl. Opt.** 48(36): 6893-6906.Li, S., Su, X., Chen, W., and Xiang, L. (2009). Eliminating the zero spectrum in Fourier transform profilometry using empirical mode decomposition. **JOSA. A.** 26(5): 1195-1201.

Shi, B., Zhang, B., Liu, F., Luo, J., and Bai, J. (2013). Fourier Transform Profilometry in Surface Reconstruction for Fluorescence Molecular Tomography. **IEEE J. Biomed. Health Inform.** 17(3): 681-689.

Takeda, M., Ina, H., and Kobayashi, S. (1982). Fourier-transform method of fringe-pattern analysis for computer-based topography and interferometry. **JOSA.** 72(1): 156-160.

Takeda, M., and Mutoh, K. (1983). Fourier transform profilometry for the automatic measurement of 3-D object shapes. **Appl. Opt.** 22(24): 3977-3982.

Watkins, L. R. (2012). Review of fringe pattern phase recovery using the 1-D and 2-D continuous wavelet transforms. **Opt. Lasers Eng.** 50(8): 1015-1022.

Yan, Z., Miyamoto, A., and Jiang, Z. (2009). Frequency slice wavelet transform for transient vibration response analysis. **Mech. Syst. Signal Process.** 23(5): 1474-1489.

Yi, J., and Huang, S. (1997). Modified fourier transform profilometry for the measurement of 3-D steep shapes. **Opt. Lasers Eng.** 27(5): 493-505.

Zhong, J., and Weng, J. (2004). Spatial carrier-fringe pattern analysis by means of wavelet transform: wavelet transform profilometry. **Appl. Opt.** 43(26): 4993-4998.

Zhong, J., and Weng, J. (2005). Phase retrieval of optical fringe patterns from the ridge of a wavelet transform. **Opt. Lett.** 30(19): 2560-2562.

CURRICULUM VITAE

Name Mr. Taweesak Chaiyakhan

Date of Birth June 15, 1990

Place of Birth Kalasin, Thailand

Address House No. 145, Village No. 9, Nong Hang sub-district, Kuchinaria district, Kalasin province, 46110, Thailand. Mobile. 66-98-2704322

Email Peck_1506@hotmail.com

Education background

- Bachelor of Science (2009 - 2013)

  Department of Physics, Faculty of Science, Khonkaen University, Khonkaen, Thailand.

  Advisor: Asst. Sayam Chutin

Publications Chaiyakhan, T., et al. (2018) Study of 3D Profilometry by using wavelet filter. In Proceedings of SPIE-The Third International Conference on Photonic Solutions. Vol. 10714, 107140J.

Grants and Fellowships

- External grants and scholarships for graduate students from Institute of Research and Development, Suranaree University of Technology.